

JGR Solid Earth

RESEARCH ARTICLE

10.1029/2020JB020763

Special Section:

Ophiolites and Oceanic Lithosphere, with a focus on the Samail ophiolite in Oman

Key Points:

- Micro to regional scale study of low-T brittle-ductile deformation in serpentinites from the Southern Troodos Transform Fault Zone
- Deformation involves a microstructural progression toward increasingly well-foliated shear zone rocks with increasing shear strain
- Fluid flow and deformation result in progressive weakening and creeping behavior with the potential to host local coseismic slip

Supporting Information:

Supporting Information may be found in the online version of this article.

Correspondence to:

S. Cox,
coxs8@cardiff.ac.uk

Citation:

Cox, S., Fagereng, Å., & MacLeod, C. J. (2021). Shear zone development in serpentinitized mantle: Implications for the strength of oceanic transform faults. *Journal of Geophysical Research: Solid Earth*, 126, e2020JB020763. <https://doi.org/10.1029/2020JB020763>

Received 13 AUG 2020

Accepted 19 APR 2021

© 2021. The Authors.

This is an open access article under the terms of the [Creative Commons Attribution License](https://creativecommons.org/licenses/by/4.0/), which permits use, distribution and reproduction in any medium, provided the original work is properly cited.

Shear Zone Development in Serpentinitized Mantle: Implications for the Strength of Oceanic Transform Faults

Sophie Cox¹ , Åke Fagereng¹ , and Christopher J. MacLeod¹ 

¹School of Earth and Environmental Sciences, Cardiff University, Cardiff, UK

Abstract Oceanic transform faults display fewer and smaller-magnitude earthquakes than expected for their length. Several mechanisms have been inferred to explain this seismic slip deficit, including increased fault zone damage resulting in elevated fluid flow, and the alteration of olivine to serpentine. However, to date, these possible mechanisms are not supported by direct observation. We use micro to kilometer scale observations from an exhumed oceanic transform fault in the Troodos Ophiolite, Cyprus, to determine mineral-scale deformation mechanisms and infer likely controls on seismic behavior of serpentinitized lithospheric mantle in active oceanic transform faults. We document a range of deformation fabrics including massive, scaly and phyllonitic serpentinite, attesting to mixed brittle-ductile deformation within serpentinite shear zones. The progressive development of a foliation, with cumulative strain, is an efficient weakening mechanism in scaly and phyllonitic serpentinite. Further weakening is promoted by a transition in the serpentine polytype from lizardite-dominated massive and scaly serpentinites to chrysotile-dominated phyllonitic serpentinite. The development of a foliation and polytype transition requires dissolution-precipitation processes. Discrete faults and fractures locally crosscut, but are also deformed by, foliated serpentinites. These brittle structures can be explained by local and transient elevated strain rates, and play a crucial role in strain localization by providing positive feedback for dissolution-precipitation by increasing permeability. We propose that the evolution in structure and deformation style documented within the serpentinitized lithospheric mantle of the Southern Troodos Transform Fault Zone is a viable explanation for the dominantly creeping behavior and long-term weakness of oceanic transform faults.

1. Introduction

Oceanic transform faults offset mid-ocean ridge segments for up to hundreds of kilometers. Therefore, according to scaling relationships between fault length and earthquake magnitude (Wells & Copper-smith, 1994), they are expected to produce relatively frequent, large earthquakes. For example, assuming a 25 km thick seismogenic zone (e.g., Prigent et al., 2020), rupture of a 200 km long, vertical transform fault would produce an $M_w \sim 8$ earthquake. Yet, despite their length and the fact they crosscut the brittle crust, geophysical observations show they host fewer and smaller earthquakes (rarely $\geq M_w 7.0$) than expected, and globally about 85% of their displacement occurs by aseismic creep (Boettcher & Jordan, 2004). Typically, oceanic transforms are difficult to study geologically, compared to continental transforms, with geological data often limited to seafloor sampling including dredges, dives and borehole observations.

The base of the seismogenic zone, defined as the depth range where earthquakes can nucleate, has been correlated with the 600°C isotherm based on the comparison of numerical thermal models and the depth limit of earthquake focal depths (Abercrombie & Ekström, 2001; Roland et al., 2010). This thermal control coincides with a change to ductile, velocity-strengthening behavior in olivine as extrapolated from laboratory deformation data (Boettcher et al., 2007). Recent studies, however, show that fluid-driven weakening and strain localization may change the dominant rheology (Kohli & Warren, 2020; Prigent et al., 2020). In addition, the ratio between the observed seismic moment and that expected from plate tectonic models (seismic coupling, χ ; Scholz, 2002) varies along strike (e.g., Braunmiller & Nábělek, 2008) and between (e.g., Boettcher & Jordan, 2004) oceanic transforms without accompanying changes in inferred thermal structure. For example, along the East Pacific Rise most oceanic transforms accommodate displacement almost entirely aseismically, with a $\chi < 0.2$ (Boettcher & Jordan, 2004).

The spatial distribution of seismic and aseismic behavior can vary along strike (e.g., Froment et al., 2014) and down dip (e.g., Kuna et al., 2019). The observation of aseismic slip within the thermally defined seismogenic zone implies that thermal structure alone cannot explain the distribution of seismicity. Several processes have been suggested to promote creep along oceanic transforms, including: (1) hydration of olivine to serpentine and other frictionally weak minerals, which can favor creep behavior (Boettcher & Jordan, 2004; Moore et al., 1997), (2) elevated fluid pressures reducing seismic coupling (Scholz, 1998), (3) deep fluid flow leading to progressive formation of weak mylonitic shear zones (Kohli & Warren, 2020; Prigent et al., 2020) and (4) increased fault zone damage resulting in locally enhanced porosity, favoring swarms of microseismicity rather than large earthquakes (Froment et al., 2014; McGuire et al., 2012). However, it is unclear which, or what combination of these processes, if any, are responsible for the lack of seismicity observed along modern transforms at temperatures <600°C.

The existing models for the seismic behavior of transform faults lack constraints by direct geological observation. Several recent papers have attempted to address this observational gap by examining the deformation history of samples dredged from modern oceanic transform faults (Kohli & Warren, 2020; Prigent et al., 2020) and collected from an exhumed transform fault (Bogota Peninsular shear zone) in the Massif du Sud ophiolite in New Caledonia (Chatzaras et al., 2020). However, these studies have focused on relatively high-temperature deformation (>600°C), and are therefore more relevant to deformation occurring beneath the inferred thermally controlled seismogenic zone. The temperature and depth limitations of these studies can be addressed using observations from the Southern Troodos Transform Fault Zone (STTFZ), Cyprus, where we are able to make micro to km scale observations of exhumed rocks deformed within the inferred thermally controlled seismogenic zone. The STTFZ is a unique example of an intact oceanic transform fault zone preserved on-land, and hence presents a unique opportunity to characterize the deformation and inferred rheology of serpentinite shear zones (SSZs) within the kinematic context of strike-slip faulting (Figure 1).

Rock deformation experiments indicate that the presence of serpentine can strongly influence rheology. Experimental studies, simulating conditions from the shallow crust to depths equivalent to ~8 GPa and 800°C, indicate a low frictional strength for serpentine, with a friction coefficient as low as $\mu = 0.1$ at room temperature (Moore et al., 1997; Reinen, 2000; Reinen et al., 1991). Previous studies have used serpentine's low frictional strength and velocity-strengthening behavior extrapolated to geological strain rates (Moore et al., 1997; Moore et al., 2004; Reinen et al., 1991, 1994) to explain fault zone weakness, strain localization and aseismic creep along many major faults including the San Andreas Fault System (Andreani et al., 2005; Irwin & Barnes, 1975; Moore et al., 1996; Moore & Rymer, 2007), in subduction zones (Hilaret et al., 2007; Hirauchi et al., 2010; Tarling et al., 2019), as well as along several oceanic transforms (e.g., Boettcher et al., 2007; Boettcher & Jordan, 2004; Froment et al., 2014; Hirth & Guillot, 2013; Kuna et al., 2019; McGuire et al., 2012).

Here we investigate the progressive development of serpentinite deformation fabrics within well-exposed SSZs in the pervasively serpentinitized lithospheric mantle of the STTFZ. Based on our field and microstructural observations, we propose a model of strain-controlled evolution of fault-rock fabric from massive serpentinite through the formation of a scaly fabric, and, ultimately, phyllonitic serpentinite. We use the term “phyllonitic” to represent a closely spaced, penetrative foliation defined by the preferential orientation of fine-grained fibrous or platy minerals. This definition is consistent with recent studies and texts (e.g., Collettini et al., 2011; Fossen, 2016; Mével, 2003; Smith et al., 2011). Similar serpentinite fabrics have previously been referred to as schistosity (e.g., Andreani et al., 2005; Hirauchi & Yamaguchi, 2007; Wicks & Whittaker, 1977); however, the term “schist” is typically reserved for coarser grained rocks with cm-scale foliation spacing (e.g., Fossen, 2016) and we therefore adopt the term that better emphasizes the fine grain size and small foliation spacing characteristic of the rocks we observe. Finally, using the progressive model we derive, we discuss the spatiotemporal distribution of deformation within the serpentinitized lithospheric mantle and the potential controls on the geophysically observed seismic behavior and rheology of active oceanic transform faults.

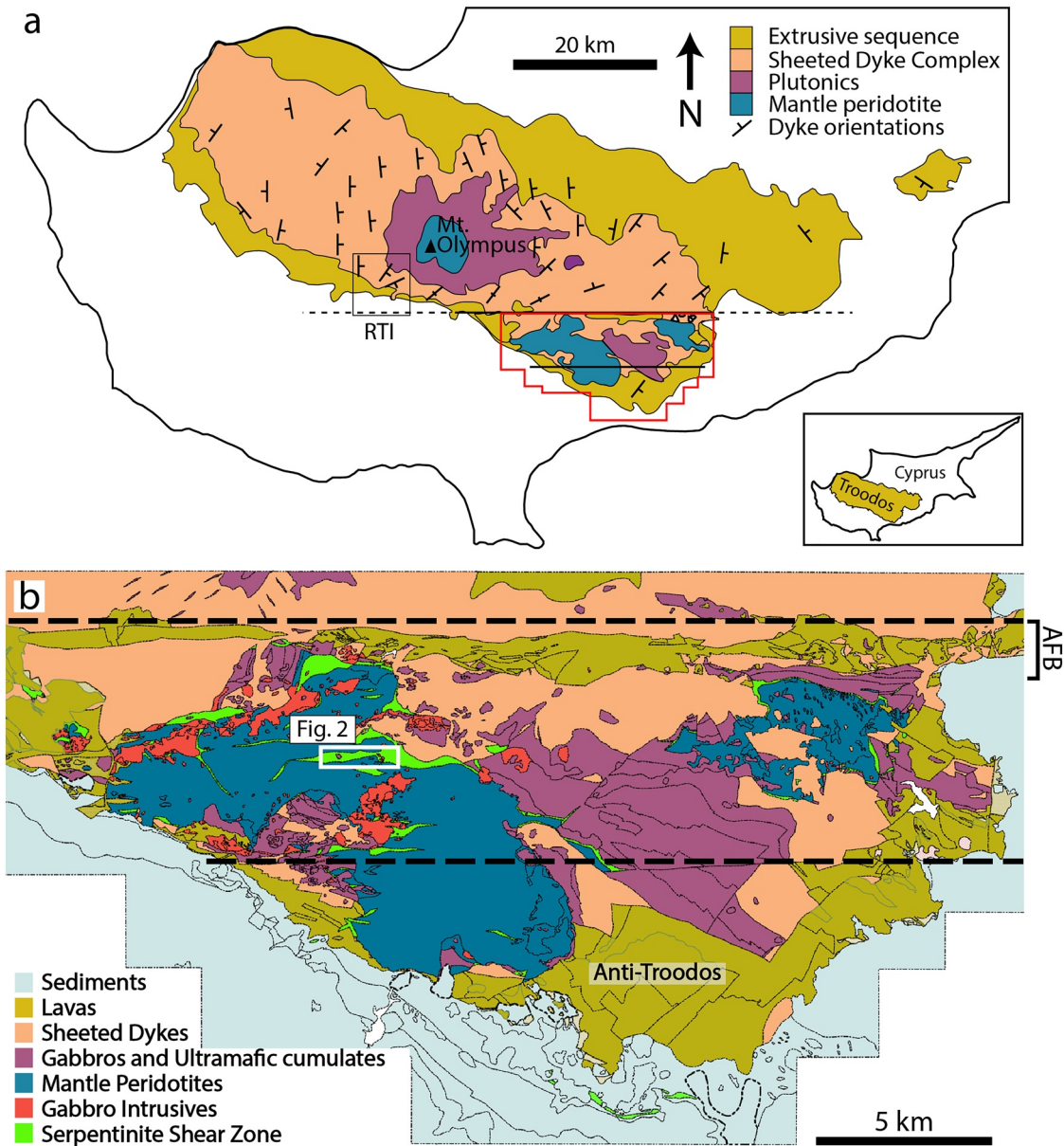


Figure 1. (a) Outline of the Troodos Ophiolite geology, Cyprus, showing deeper stratigraphic levels exposed in the center of the ophiolite (Mount Olympus) (after Fagereng and MacLeod [2019]). The Southern Troodos Transform Fault Zone is located at the southern margin of the ophiolite, within the region known as the Limassol Forest Complex (outlined in red). Dyke orientations are shown north of the transform-tectonized zone reflecting clockwise rotation of the dykes. RTI – ridge-transform intersection from MacLeod et al. (1990). (b) Detailed geological map of the Limassol Forest Complex showing the “Southern Troodos Transform Fault Zone” and the approximate limit (dashed lines) of oceanic transform fault deformation (after Gass et al., 1994). The Southern Troodos Transform Fault Zone, which includes the E-W trending Arakapas Fault Belt (AFB; the northern limit of transform deformation) and much of the Limassol Forest Complex, was originally mapped at 1:5000 scale by Simonian (1975), Murton (1986b), and MacLeod (1988). “Anti-Troodos” refers to a fragment of non-transform-tectonized crust identified as lying on the opposite side of the transform fault zone (MacLeod, 1990). The white box in (b) shows the location of Figure 2.

2. Geological Setting of the Southern Troodos Transform Fault Zone

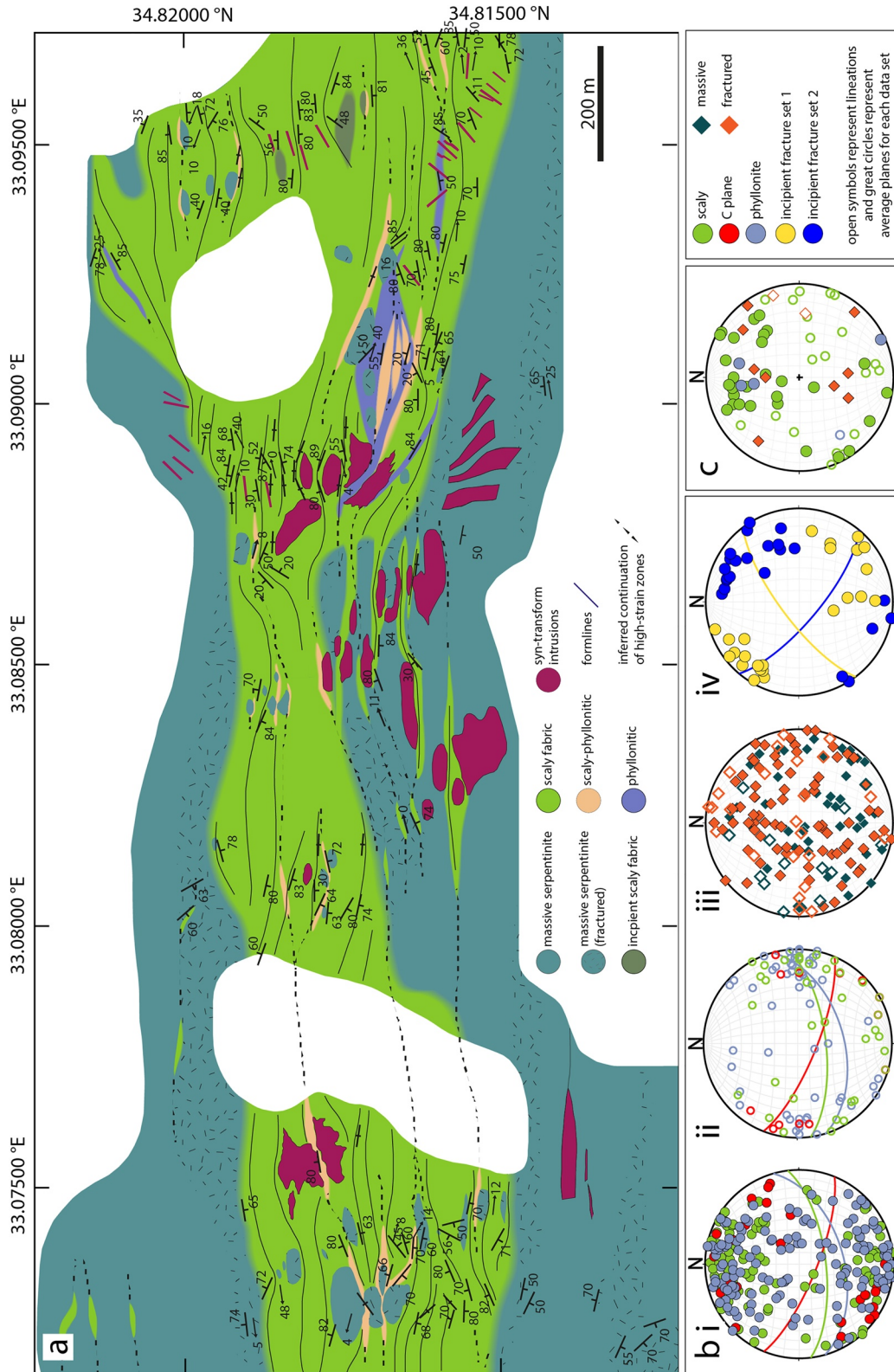
The Troodos Ophiolite of Cyprus is a fragment of Late Cretaceous oceanic lithosphere, which formed in a supra-subduction zone setting (e.g., Mukasa & Ludden, 1987; Pearce, 1975; Robertson et al., 2012) and was exhumed during the latest Cretaceous to Miocene (e.g., Robertson, 1977). The southern margin of the Troodos Ophiolite has been disrupted by ocean-floor (presediment) strike-slip faulting in the Limassol Forest Complex and Arakapas Fault Belt (Figure 1), perpendicular to the broadly N-S trend

of sheeted dykes in the main Troodos Ophiolite. Together, these areas are interpreted as representing a dextral oceanic transform fault zone, termed the Southern Troodos Transform Fault Zone (STTFZ) (Gass et al., 1994; MacLeod & Murton, 1995). The STTFZ has an exposed thickness of ≥ 5 km and is traceable for >60 km along strike (Gass et al., 1994; MacLeod & Murton, 1993, 1995; Moores & Vine, 1971; Murton, 1986a, 1986b; Simonian & Gass, 1978). 1:5000 Scale field mapping of the entire Limassol Forest Complex and Arakapas Fault Belt by Simonian (1975), Murton (1986b), and MacLeod (1988) (reported in Gass et al. [1994]) has allowed ocean-floor deformation and kinematics to be identified and deconvolved from that relating to the emplacement and exhumation of the ophiolite. Later detachment and thrust faulting locally overprints, and is distinct from, transform-related structures in the Limassol Forest Complex and Arakapas Fault Belt (Gass et al., 1994; MacLeod, 1990). The outcrops we study here have been chosen to avoid the later deformation overprint and to represent structures kinematically consistent with transform faulting.

In the southern-most 5–15 km of the main Troodos ophiolite, immediately north of the Arakapas Fault Belt (Figure 1a), dyke orientations rotate clockwise toward the main transform fault, from N-S strikes toward E-W (Simonian & Gass, 1978). Paleomagnetic studies (e.g., Bonhommet et al., 1988) show that this dyke swing records clockwise vertical-axis rotations that may be explained by drag on a dextrally slipping transform. MacLeod et al. (1990) showed that these rotations were imparted entirely at the inside-corner ridge-transform intersection (<5 km from the ridge axis; Figure 1a). This rotation was then frozen in place and translated passively once the strain was partitioned onto the main STTFZ. Therefore, the dyke rotation region does not simply reflect a 5–15 km wide STTFZ damage zone. The main transform-related deformation is within the ~ 5 km-wide STTFZ and is typically localized into steeply dipping, E-W striking features within the crust and lithospheric mantle of the ophiolite.

Whilst abundant deformation is also documented in the crustal section (e.g., Fagereng & MacLeod, 2019; MacLeod, 1990; MacLeod & Murton, 1993), the focus of this paper is specifically on mechanisms of deformation within the mantle lithosphere. Deformation of lithospheric mantle rocks is hosted in anastomosing SSZs that are ≤ 500 m wide and traceable for ≤ 12 km along strike (lime green in Figures 1 and 2), displaying brittle and ductile deformation of serpentinite to various intensities (Fagereng & MacLeod, 2019; MacLeod & Murton, 1993; Murton, 1986a). Serpentinization of STTFZ mantle rocks initiated early and is nearly pervasive, probably $>95\%$ down to several km depth. Mapping by MacLeod and Murton (1993) suggests that the degree of serpentinization is higher in SSZs and decreases into less deformed wall-rock. Many SSZs contain isolated wehrlite and gabbro plutons with associated dykes, interpreted as a suite of (boninitic) intrusions that were coeval with the transform-related deformation (MacLeod & Murton, 1993, 1995; Murton, 1986a). Mutually cross-cutting relationships between STTFZ deformation and Transform Sequence intrusions led Murton (1986a), MacLeod and Murton (1993), and MacLeod and Murton (1995) to hypothesize that the STTFZ was, at least locally, transtensional and “leaky.”

The original preserpentinization lithology that constitutes the mantle lithosphere within the STTFZ is predominantly harzburgite ($>90\%$; Gass et al., 1994). Dunite is present in the form of m- to 10-m-scale pods, or as massive dunite (hundreds to m-scale) in the NE Limassol Forest Complex. Although all are now pervasively or near-pervasively serpentinized, the original lithology can normally be recognized if shearing is absent. Orthopyroxene in harzburgite is replaced by bastite, which may be elongated and sometimes outline an original, steeply dipping, high-temperature tectonite fabric. In a high proportion of cases, however, serpentinization obscures evidence for earlier fabrics. Dunite is completely serpentinized and can be distinguished from a harzburgite protolith by the lack of bastites and higher proportion ($< a$ few percent) of lustrous Cr-spinel. These porphyroclastic fabrics were interpreted as remnants of high-temperature deformation that formed in the convecting asthenosphere (Gass et al., 1994; Murton, 1986b), and are comparable to L-S tectonic fabrics found in most mantle peridotites (e.g., Ceuleneer et al., 1988). These asthenospheric fabrics trend predominately NW/NNW on the km-scale and document a clockwise rotation toward an E-W foliation in the western Limassol Forest Complex (Murton, 1986b). They are distinguished from the discrete, localized and more intensely foliated shear zones that are restricted to the STTFZ and are predominately E-W striking and steep. The asthenospheric fabrics are commonly crosscut by E-W striking SSZs, ruling out their control on the localization of SSZs within the STTFZ (Gass et al., 1994).



3. Methods

In order to constrain the conditions and evolution of transform-related deformation in the mantle lithosphere of the STTFZ, microstructural observations were made on standard 30 μm thick polished thin sections. We chose samples representative of the various deformation styles observed at the macroscale. Incohesive samples were set using Epofix cold-setting embedding resin, a low-fluorescence epoxy, and cut along a sub-horizontal plane containing the slip vector and maximum asymmetry. Thin sections were studied using a range of optical microscope, scanning electron microscope (SEM) and Raman spectroscopy methods.

3.1. Raman Spectroscopy

Raman spectroscopy was used to identify the serpentine polytypes (e.g., Rooney et al., 2018) and Raman spectroscopy mapping was conducted using an Alpha 300R + confocal Raman microscope (WITec GmbH, Ulm, Germany) in the Chemistry department of Otago University, New Zealand, following procedures of Rooney et al. (2018) and Tarling et al. (2019).

3.2. Scanning Electron Microscope

Energy-dispersive X-ray spectroscopy (EDS) maps were produced from polished thin sections coated in 10–15 nm of carbon. Data were acquired using a Zeiss Sigma HD Field Emission Gun Analytical scanning electron microscope (SEM) fitted with two Oxford Instruments 150 mm² energy dispersive X-ray spectrometers in the School of Earth and Environmental Sciences at Cardiff University. EDS mapping was carried out at an accelerating voltage of 20 kV with a nominal beam current of 4.3 nA under a high vacuum.

4. Results

4.1. Macroscopic Field Observations

Mapping of an $\sim 2 \text{ km}^2$ area of the exposed mantle section within the Limassol Forest Complex reveals that deformation is heterogeneously distributed, with intensity varying on a meter to kilometer scale (Figure 2). The particular shear zone mapped here displays an anastomosing tectonic fabric with an average moderate to steeply dipping foliation striking $\sim \text{E-W}$ (083/67° S) and gently plunging lineation ($< 30^\circ$), consistent with sub-seafloor deformation under conditions associated with an oceanic transform fault, and distinct from structures associated with later uplift and exhumation (Figure 2b). From our field observations, we divide the serpentinite into five groups based on their macroscale fabrics (Figure 3).

- (0) *Massive serpentinite* comprises a blocky texture with variably oriented fractures, cm to m long and spaced at a similar scale. Primary olivine and orthopyroxene are rare ($< 1\%$), with serpentinite after olivine and elongate bastite pseudomorphs ($< 1 \text{ cm}$ in length) after orthopyroxene (Figure 4a). Massive serpentinite dominates the mantle section away from SSZs and within SSZs it commonly occurs as pods surrounded by scaly and phyllonitic fabrics.
- (i) *Intensely fractured serpentinite* is comparable to the massive serpentinite described above, but with an increased number of fractures without a preferred orientation. Fractured serpentinite is most common near the margins of well-developed SSZs (Figures 2a and 2b).
- (ii) *Incipient scaly serpentinite* is also similar to massive serpentinite, but contains two discrete, $< 2 \text{ cm}$ thick, planar fracture sets that intersect at a high angle (typically $\sim 80^\circ$) to form rhomboidal blocks

Figure 2. (a) Detailed geological map (WGS84) of the internal structure and variable distribution of deformation fabrics within a serpentinite shear zone in the Limassol Forest Complex (white box in Figure 1b). The map highlights areas of scaly and phyllonitic fabric, pods of massive to fractured serpentinite and transform sequence intrusions (dykes – drawn as far as observed). (b) Orientations of the fabrics mapped in (a) are summarized in lower hemisphere, equal area stereonet of (i) poles to planes of S-C fabrics from scaly and phyllonitic serpentinite, (ii) lineations from the serpentinite shear zone with great circles showing average foliations from (i), (iii) lineations and fractures in massive and fractured serpentinite, and (iv) fractures in the incipient scaly fabric. (c) shows detailed measurements of fractures and scaly foliation from a 10 m wide localized shear zone dominated by a scaly to phyllonitic fabric. Descriptions of the various serpentinite fabrics are in Section 4.1.

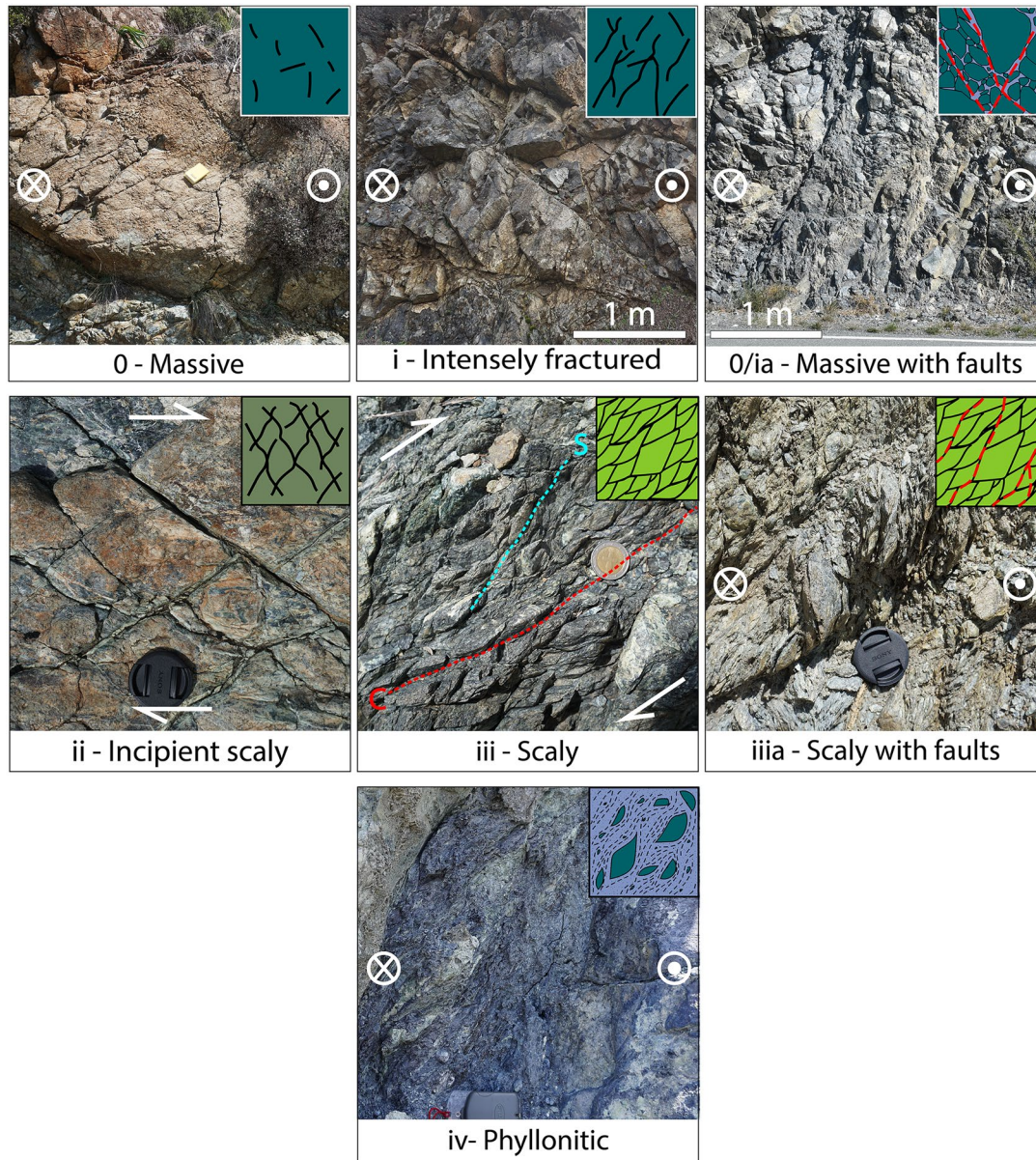


Figure 3. Descriptive categorization of deformation styles observed in the Southern Troodos Transform Fault Zone serpentinitized lithospheric mantle with schematic representations. (0) massive serpentinite (near WGS84: 34.81282°N 33.07059°E); (i) intensely fractured (near 34.81282°N 33.07059°E); (0/ia) (near 34.77545°N 33.08063°E); (ii) (near 34.81925°N 33.09573°E); (iii) (near 34.79322°N 33.08681°E); (iiiia) (near 34.81586°N 33.07257°E); (iv) (near 34.80666°N 33.00415°E). Color scheme as in Figure 2.

(Figure 2b). The fractures are in places filled with fibrous serpentine, reflecting either extensional or transtensional opening.

- (iii) *Scaly serpentinite* defines individual serpentinite phacoids by a network of anastomosing disjunctive cleavage (e.g., Shervais et al., 2005; Vannucchi et al., 2003). Phacoids are variably sized (cm to dm) with polished surfaces. They are commonly asymmetric with sub-horizontal, E-W trending long axes. Their short axes are predominantly sub-horizontal and trend N-S. The alignment of phacoids in this way defines an E-W striking sub-vertical foliation. Discrete shear planes crosscut the foliation at an angle of $\sim 30^\circ$ (Figure 2b) giving an S-C-like geometry (Figure 3iii), which is almost always consistent with dextral slip on steeply dipping planes. Serpentinite phacoid surfaces commonly contain a coating of fibrous serpentine recording shear deformation with a locally variable orientation (Figure 4c). Fibrous

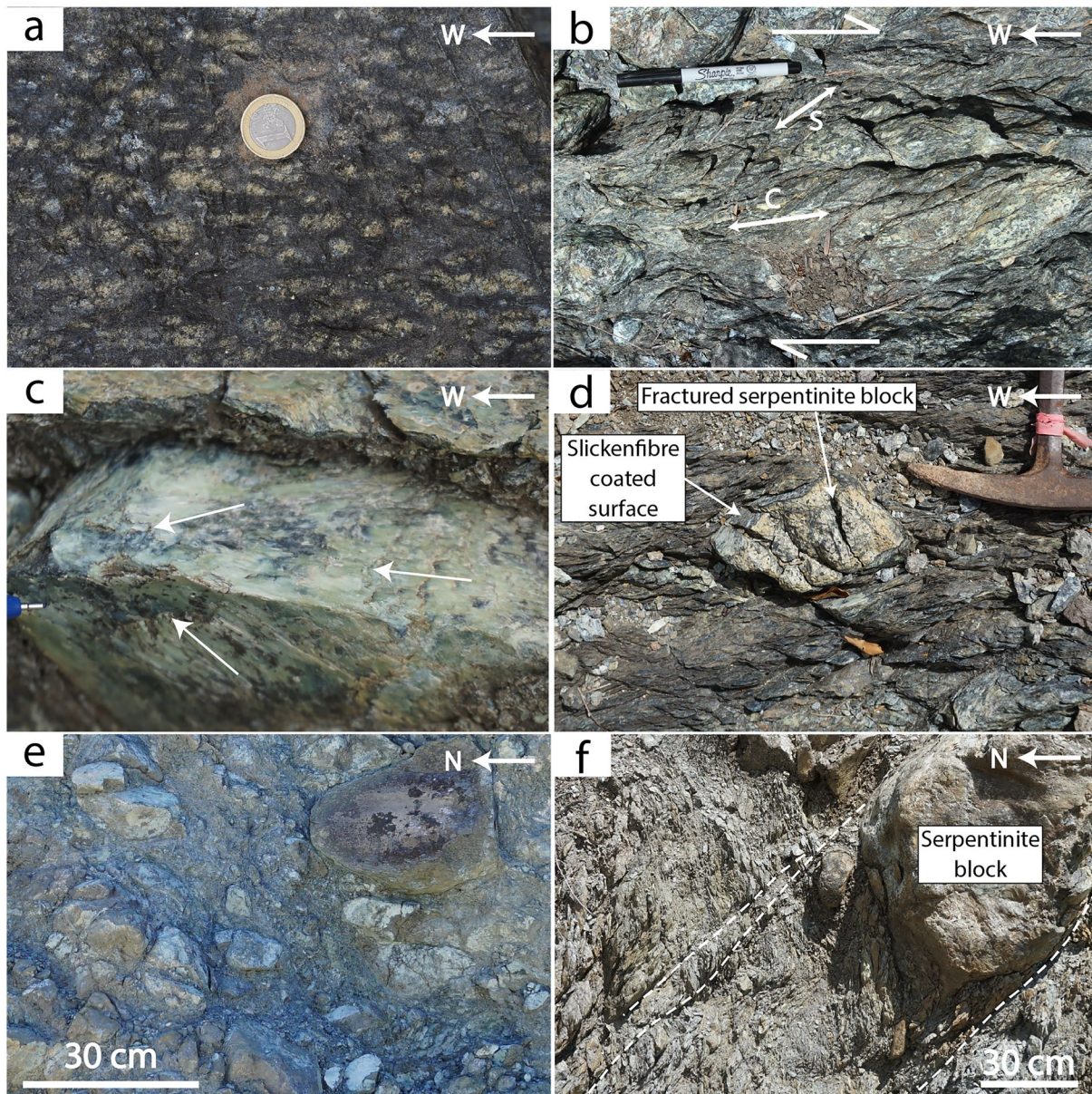


Figure 4. Structures recorded within serpentinite shear zones. (a) Steeply dipping porphyroclastic fabric (defined by bastite pseudomorphs after orthopyroxene) within massive serpentinite pseudomorphing the highest temperature ductile deformation in the Southern Troodos Transform Fault Zone (near WGS84: 34.77512°N 33.08082°E). (b) Typical scaly serpentinite with an S-C fabric (near 34.79214°N 33.08608°E). (c) Slickenfibre-coated phacoid making up the scaly fabric (near 34.81699°N 33.08106°E). (d) Fractured serpentinite block within a scaly serpentinite zone (near 34.81771°N 33.10985°E). (e) Phyllonitic serpentinite with a block-in-matrix type fabric (near 34.77396°N 33.07844°E). (f) Discrete plane parallel to the edge of a serpentinite block cutting scaly serpentinite (near 34.81588°N 33.07256°E). (a–d) look at horizontal surfaces; (e–f) are looking at approximately vertical cliffs.

serpentine may also form lineations on C planes. Fractured serpentinite phacoids are common (Figure 4d), with some fractures containing crack-seal veins.

- (iv) *Phyllonitic serpentinite* is defined by a narrowly (<2 mm) spaced cleavage that is more planar than in scaly serpentinite, with S and C planes effectively parallel. Serpentinite phacoids are present but isolated (Figure 4e). Other, more angular blocks of serpentinite and Transform Sequence intrusions can also be found within the phyllonitic fabric, forming a block-in-matrix fabric. Phyllonitic zones form relatively narrow anastomosing strands up to 10 m in total thickness and can be traced for ~300 m along strike (Figure 2). Phyllonites can also occur more locally as tabular, <1 m wide zones at the boundaries between scaly and massive serpentinite.

The various serpentinite groups highlight that mixed-mode deformation is common in the STTFZ lithospheric mantle. It is also apparent that variations along and across strike between dominantly brittle, mixed brittle-ductile and dominantly ductile deformation regions exist (Figure 5). We use the term “ductile” to describe spatially continuous deformation at the outcrop scale (Figures 3iii–3iv, 4b and 4e). This contrasts to “brittle,” which we use to define discontinuous deformation at the same scale of observation (Figures 3i–3ii, 3iia–3iia, 4d and 4f). Areas dominated by brittle deformation (Figure 5a) contain steeply dipping, E-W striking discrete faults (Figure S1), <5 cm thick, that are comparable to C planes and contain gently plunging slickenfibres. These discrete faults crosscut entire outcrops, and can be traced for up to ~10 m along strike length, limited by outcrop continuity. The total amount of slip along these discrete planes is unknown because of a lack of marker horizons. Angular blocks of serpentinite (from cm to >3 m) sit within a poorly interconnected scaly matrix in dominantly brittle zones. In contrast to these dominantly brittle zones, ductile portions are characterized by isolated, usually more rounded serpentinite blocks of various size, mm to >2 m long, set in a well-interconnected scaly to phyllonitic serpentinite matrix and without any discrete throughgoing faults (Figure 5c). Mixed brittle-ductile portions contain a relatively well-interconnected scaly matrix, and faults and fractures that in places occur parallel to block boundaries (Figures 4f and 5b). The scaly fabric and fractures define a mutually cross-cutting relationship.

The SSZs are highly complex and heterogeneous in their internal structure. However, the overall style of SSZ deformation roughly coincides with various block:matrix proportions and distributions, with areas that are more block-supported showing a higher number of obvious faults at the outcrop scale than those that are matrix-supported. However, this does not preclude many foliation-subparallel faults or faults being overprinted by ductile deformation in the more matrix-rich outcrops. Locally, the style of deformation can also relate to contrasting competency, e.g., at the boundaries of some of the largest serpentinite clasts, tabular zones of phyllonite may be documented, although that is not always the case. The deformation styles more commonly grade between one another, sometimes at the meter scale and sometimes at much larger scales.

4.2. Microscopic Observations of Serpentinite Shear Zones

The observations we make at the microscale reveal distinct microstructural groups, which are related, but not equivalent, to the serpentinite groups we defined (Section 4.1 above) at the outcrop scale where we divided the serpentinite into massive, fractured, scaly and phyllonitic serpentinite.

4.2.1. Mesh Microstructure

Massive serpentinite shows pseudomorphic mesh and bastite microstructures (Figure 6a), after olivine and pyroxene respectively, typical of hydrated oceanic peridotite (Viti & Mellini, 1998; Wicks & Whittaker, 1977). Accessory minerals include primary chrome spinel. Magnetite is present as a product of serpentinitization of olivine and most commonly concentrated at mesh rim boundaries, although also present within mesh rims and cores. Serpentinitization is pervasive and original olivine or pyroxene grains are rare.

Raman spectroscopy identifies an intensity peak at $3,683\text{ cm}^{-1}$ for mesh rims suggesting, in comparison to published Raman spectra for serpentinite polytypes (Rooney et al., 2018), that they comprise lizardite (Figure S2), while spectra from the ultrafine-grained cores reveal intensity peaks consistent with mixed chrysotile and lizardite (mesh core in Figure S2). Lizardite grains in mesh rims are <5–10 μm in size (Figure S3). Observations with a gypsum tint plate inserted in an optical microscope illuminate two, near-orthogonal crystallographic preferred orientations (CPO) of lizardite grains in mesh rims, surrounding poorly crystalline cores (Figure 6a). Viti and Mellini (1998) and Viti et al. (2018) interpret similar observations to represent variation in orientation of the (001) lizardite axes. Antigorite (Raman shift at $3,657\text{ cm}^{-1}$) is only a trace constituent of massive serpentinites (<1%) observed locally along rim boundaries (Figure S3). Bastite comprises a fine-grained serpentine, much like mesh cores, and commonly retains a pseudomorphic pyroxene cleavage. Chrysotile veins cross-cut mesh microstructures and are dominantly extensional.

4.2.2. Ribbon Microstructure

Scaly phacoids contain a ribbon microstructure in which mesh cells (one cell consists of a single mesh core with surrounding rims) are sigmoidal. Much like mesh microstructure, ribbon microstructure comprises lizardite-dominant rims and mixed lizardite-chrysotile cores. Gypsum tint plate observations highlight

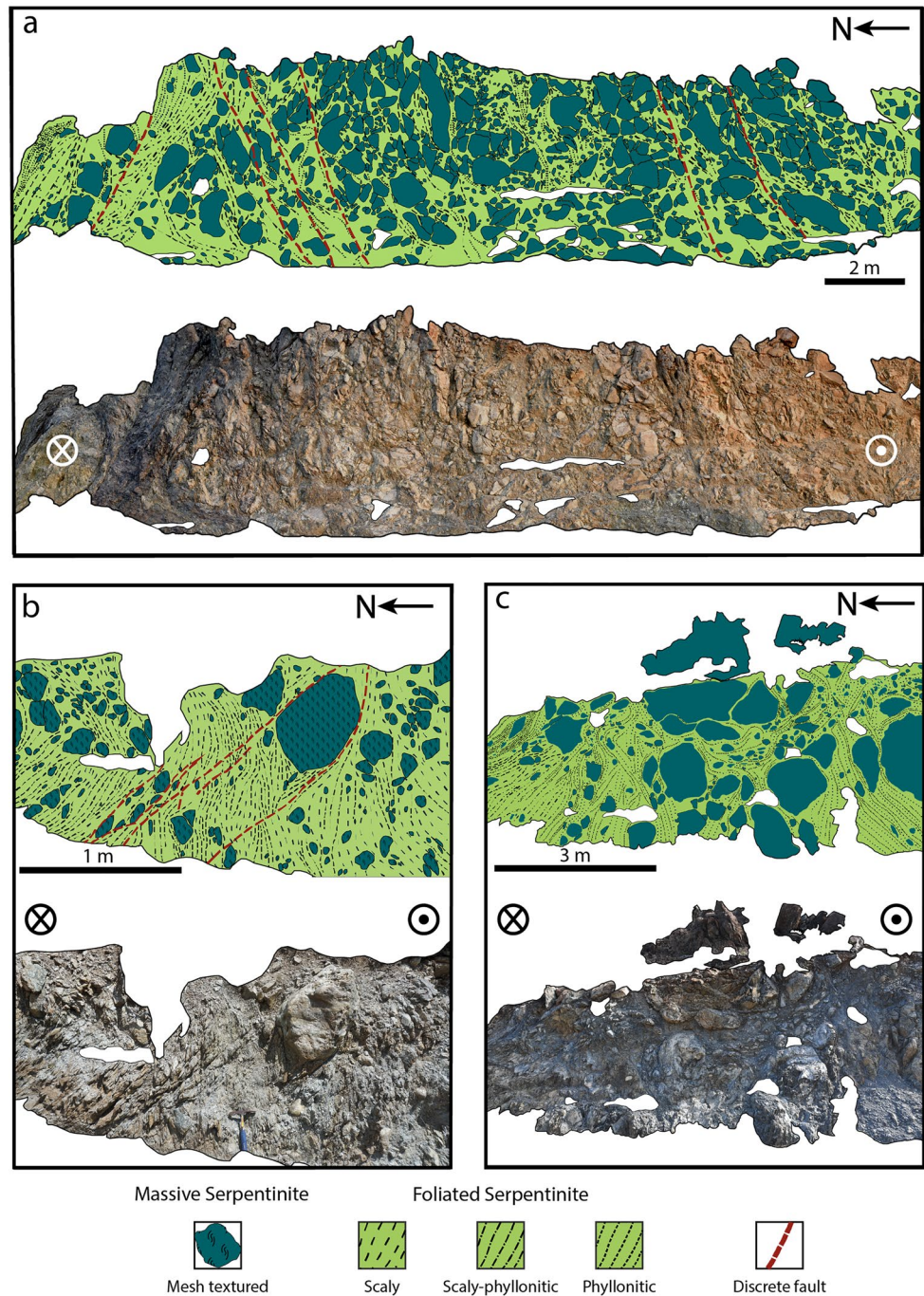


Figure 5. Roadside maps of vertical outcrop of a serpentinite shear zone, looking along the foliation towards the East, showing their highly variable nature of deformation. (a) Dominantly brittle section with multiple, discrete throughgoing planes and fractured blocks (near WGS84: 34.79214°N 33.08608°E). (b) Brittle-ductile zone with mutually cross-cutting fractures and a scaly fabric (near 34.81586°N 33.07257°E). (c) Ductile portion of the same serpentinite shear zone as (a), with a well-developed block-in-matrix fabric and phyllonitic matrix (near 34.79335°N 33.08612°E). Equal area lower hemisphere stereonet are shown in Figure S1.

one dominant rim CPO in sigmoidal ribbon cells that form a 3D interconnecting network of well-aligned lizardite, defining a foliation (Figure 6b). Ribbon cells generally comprise smaller cores than mesh cells. Magnetite grains, <10 μm , are concentrated at ribbon boundaries and defines seams traceable up to a few

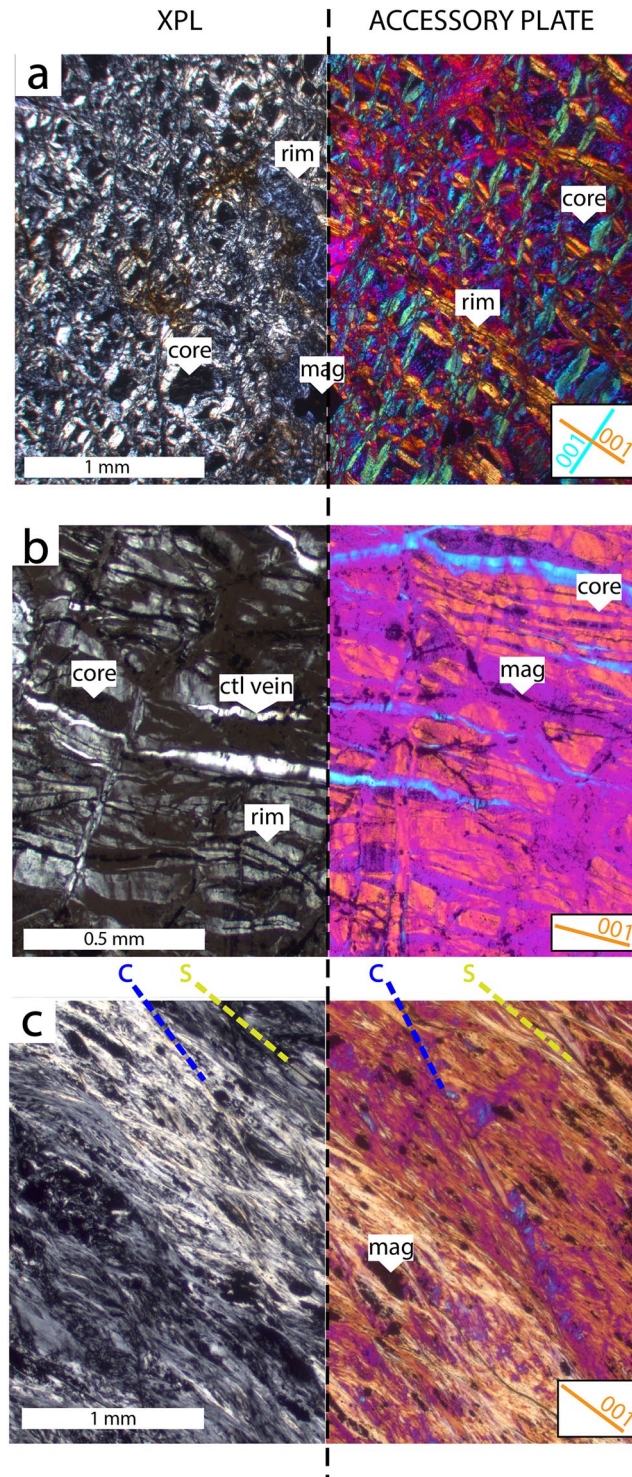


Figure 6. Serpentinite microstructures within variably deformed serpentinite. Each panel shows the left half of the image in cross-polarized light, and the right half with a gypsum tint plate. (a) Untectonized mesh microstructure. The gypsum plate illuminates pink mesh cores (core) and yellow and blue lizardite rims (rim) with near-perpendicular (001) plane orientations. (b) Ribbon microstructure (deformed mesh microstructure) with one dominant rim orientation (yellow color under the gypsum plate) and reduced core volume. This microstructure is commonly observed at the edges of serpentinite phacoids in scaly serpentinite. Seams of magnetite define the ribbon cells. (c) Phyllonite preserving no original mesh microstructure but a fibrous chrysotile schistosity with (S) and C planes (C). In (b and c), the (001) planes are parallel to the foliation, which also approximates the shear plane. The sample in (a) is not foliated. Magnetite forms as seams and concentrates into clusters within the foliation.

mm (Figure 6b). This ribbon fabric is particularly well-developed toward the edges of massive serpentinite phacoids with a mesh microstructure.

4.2.3. Fibrous Microstructure

The microstructure of phyllonitic serpentinite differs from massive and scaly serpentinite. It comprises a penetrative foliation of serpentine fibers, $<1 \mu\text{m}$ wide, with few rigid serpentinite clasts ($\sim 1 \text{ mm}$) that contain a mesh or ribbon microstructure. Reflected light images show clasts are wrapped by the foliation, and have asymmetric pressure shadows indicating dextral shear sense. SEM and optical microscope observations show the phyllonitic cleavage is defined by well-aligned serpentine fibers (Figure 6c). Fiber orientations vary in space because they are locally deflected by sub-mm clasts, but overall they are subparallel to the bulk shear plane of the STTFZ. Magnetite is distributed throughout the foliation as individual grains, asymmetric clusters, and seams up to a few mm long parallel to the foliation (Figure 6c). Phyllonitic serpentinite contains discrete C planes defined by fractures creating an S-C-like geometry at the microscale, with an acute angle between S and C planes (Figure 6c) and consistent with the inferred dextral shear sense of the STTFZ.

Raman spectroscopy identifies a spectrum with peaks at $3,692$ and $3,696 \text{ cm}^{-1}$ for serpentine fibers, consistent with chrysotile being the predominant polytype in phyllonitic serpentinites (Figures 7 and S2). Relict $\sim 10 \mu\text{m}$ sized grains of lizardite are locally present, but only in the form of scattered grains at low concentration ($<5\%$) throughout the phyllonitic foliation (Figure 7). Raman-point analysis shows mixed lizardite and chrysotile signals at the boundary between the lizardite clasts and the chrysotile foliation (Figure 7).

4.3. Comparison of Microstructure With Mineral Composition

SEM back-scatter electron (BSE) images of serpentinites showing mesh and ribbon microstructures reveal a density contrast between cores and rims (Figures 8a and 8c). The distribution of major elements within and between serpentine polytypes and fabric types should reflect the conditions of formation. Using energy-dispersive spectroscopy (EDS) we analyzed the major element composition of mesh rims, mesh cores, bastites, phyllonitic textures (chrysotile), and antigorite and lizardite clasts. Although a detailed analysis of serpentine chemistry is beyond the scope of this study, we highlight differences between serpentines of differing microstructures.

EDS analysis indicate that most, but not all, mesh rims are Mg-rich relative to their cores (Figure 8b and 8d). Conversely, most rims have lower Fe concentrations than their cores. The exception to Mg-rich and Fe-poor rims come from a single sample. Bastites are generally lower in Mg than mesh rims, comparable to mesh cores but higher in Fe compared with most serpentine after olivine (Figure 9). The chemical difference between bastite and the mesh microstructure likely relates to the initial Mg and Fe compositions of olivine and pyroxene from which they formed.

Although there are variations within our sample set, distinct chemical groups arise for each microstructure. In particular, the phyllonitic serpentinite is distinct with lower and more homogeneous Fe-, and higher Al-concentrations (Figure 9), but is similar to pressure shadow material adjacent to massive serpentine phacoids. Phyllonitic serpentinites occasionally reveal a density contrast in BSE images, mimicking the scaly fabric and consistent with variations in Mg content (Figures 8e and 8f). Relict lizardite grains within phyllonitic serpentinite are similar in size and have compositions comparable to lizardite grains making up mesh rims (Figure 9).

5. Discussion

5.1. Conditions of Serpentinization of the Lithospheric Mantle Before and During Faulting

5.1.1. Temperature of Serpentinization and Deformation

The deformation described within SSZs in the STTFZ represents deformation in the shallow, serpentinized mantle lithosphere within the transform-tectonized zone. Almost all preserved transform-related deformation occurred when the lithospheric mantle had been or was being serpentinized. This is based on a variety of lines of evidence including transform-related lineations defined by serpentine minerals (see also Gass

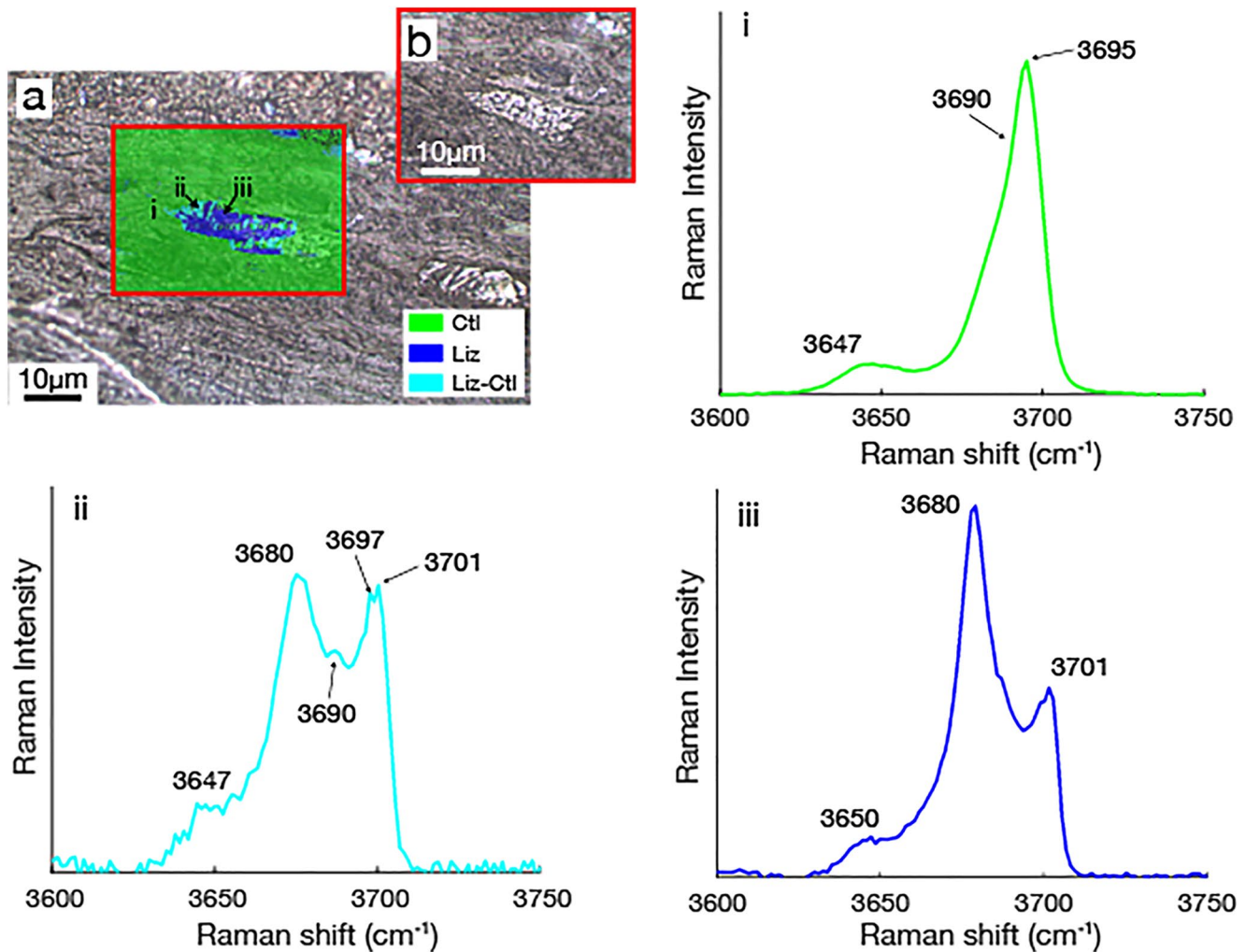


Figure 7. Raman spectroscopy point analysis and mapping of various serpentinite microstructures. (a) Raman map overlain on a reflected light image showing a lizardite grain that has partially broken down into chrysotile phyllonitic serpentinite. (b) Reflected light image of the mapped area in (a). Point spectra for each of the three locations mapped in (a) show a transition from (i) a chrysotile signal, (ii) mixed chrysotile-lizardite signal to (iii) a lizardite signal.

et al., 1994; MacLeod & Murton, 1993). The Troodos ophiolite is generally believed to have formed at a relatively slow spreading ridge (e.g., Varga & Moores, 1985), and hence the STTFZ was a slow-slipping, probably moderate-offset transform (e.g., MacLeod & Murton, 1993). The intact magmatic crustal thickness of the Troodos Ophiolite is estimated to have been 4–5 km (Gass et al., 1994), although this originally “layer-cake” magmatic crust was subject to geometrically complex tectonic dismemberment within, and up to a few km away from, the transform-tectonized zone. Crustal thickness estimates are not therefore indicative of depths of deformation beneath the seafloor. Although the mantle lithosphere deformation we document is therefore representative of depths from as much as 4–6 km below the seafloor, some of it undoubtedly took place at much shallower depths. There is, however, little or no evidence for exposure of serpentinite on the seafloor within the STTFZ (Gass et al., 1994).

The structural and mineralogical development of serpentinite within the STTFZ was progressive. Serpentinization of the mantle harzburgite likely occurred as a two-stage process (e.g., Rouméjon et al., 2018): (1) initial localized serpentinization along microfractures that are defined by planes of magnetite (Figure 6a) and also represented by lizardite-dominated mesh rims, then (2) more diffuse serpentinization, resulting in fine-grained mesh cores. Minor amounts of antigorite occur along some mesh rims in STTFZ serpentinites (Figure S3), consistent with serpentinization temperatures of >300°C along these microfractures

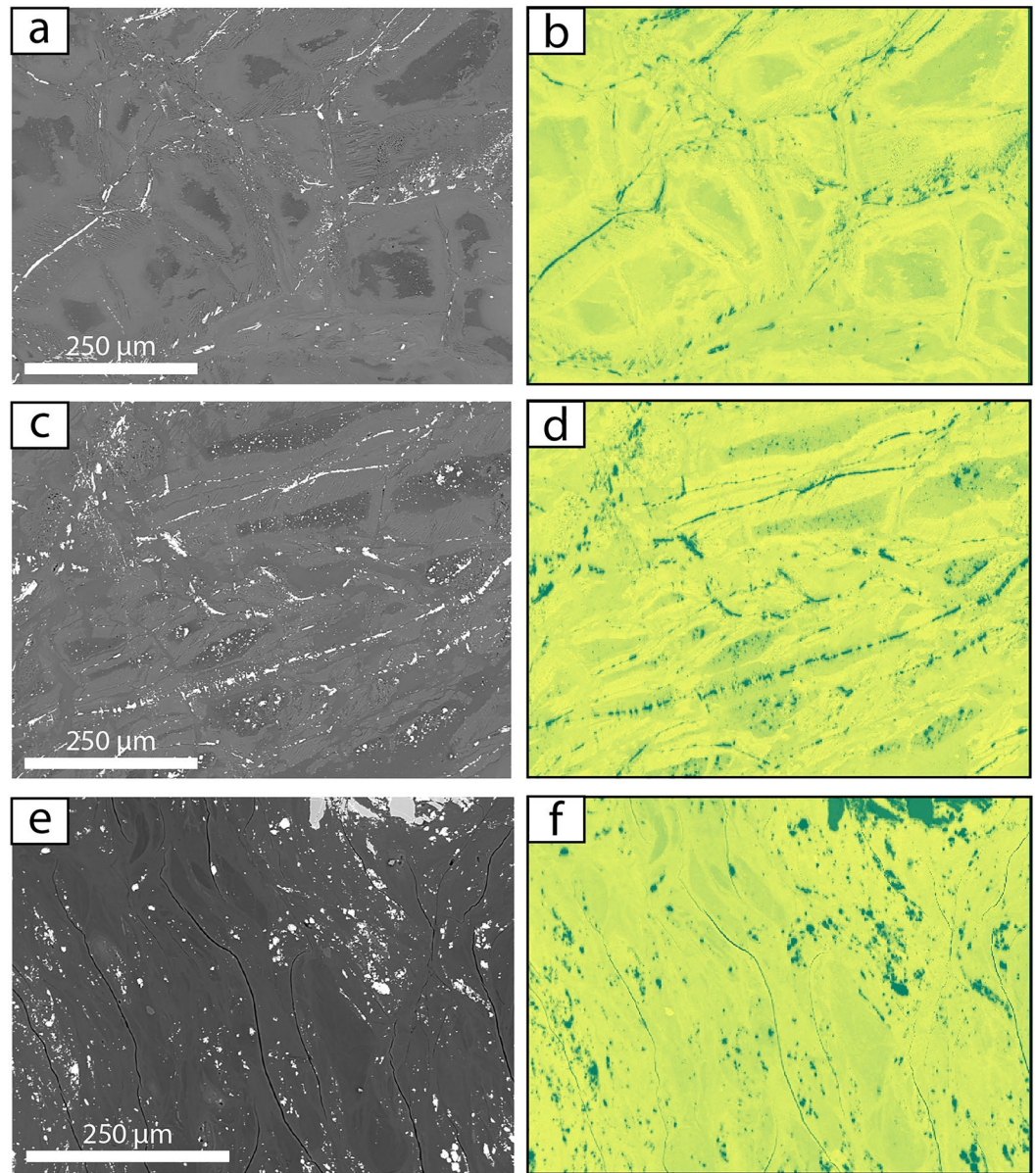


Figure 8. BSE and EDS maps of variably deformed serpentinite. (a) and (b); Mesh microstructure with Mg-rich rims and Mg-poor cores. (c) and (d); Ribbon microstructure displaying a similar chemical variation between rims and cores as in (b). (e) and (f); Phyllonitic serpentinite with Mg variations illuminating a scaly fabric. Green = low MgO counts, yellow = high MgO counts.

(Evans, 2004). Mesh microstructures comprising lizardite and chrysotile are known to form directly from the serpentinization of olivine, whereas antigorite typically forms a distinct interpenetrating texture (Wicks & Whittaker, 1977). As the untectonized serpentinized harzburgites of both the central Troodos (Mount Olympus) and Limassol Forest (STTFZ) outcrops (Figure 1a) are dominated by lizardite and chrysotile mesh texture serpentine, we suspect that they record the initial serpentinization of the peridotite (harzburgite and dunite). If the lizardite-chrysotile mixture overprinted an earlier antigorite serpentine, at least some evidence of interpenetrating textures should have been preserved. The occurrence of minor amounts of antigorite suggests that pressure and temperature conditions during the initial serpentinization were within the range where antigorite, lizardite and chrysotile coexist. At the relatively low pressures expected for the shallow mantle setting, lizardite and chrysotile are stable at $<400^{\circ}\text{C}$, and antigorite at $>300^{\circ}\text{C}$

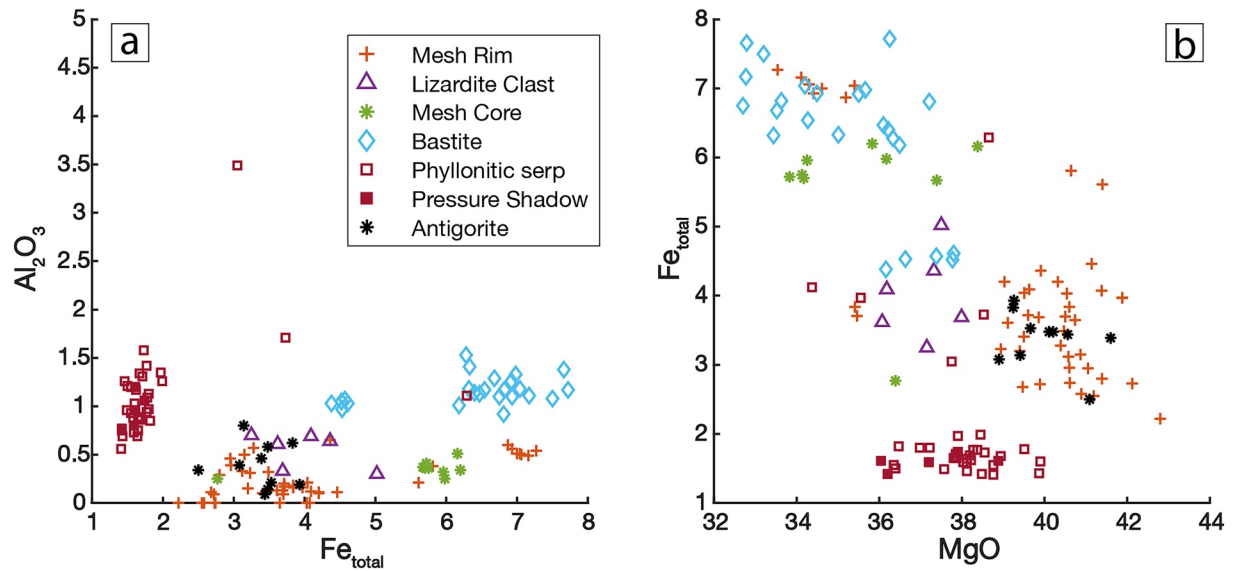


Figure 9. Plots from quantitative EDS point analyses of oxide weight percent from different serpentinite microstructures. (a) Al_2O_3 versus total Fe (as in Fe_2O_3 and FeO) and (b) total Fe versus MgO plots showing each microstructure as chemically distinct and relatively internally homogeneous. A small cluster of relatively high-Fe, low-Mg mesh rims is an exception to these distinct and homogeneous groups. Chrysotile phyllonite contains lower Fe and higher Al than the serpentine making up mesh microstructures.

(Evans, 2004). These constraints suggest the initial serpentinization occurred at lower greenschist facies conditions, 300°C – 400°C . In scaly and phyllonitic serpentinite, lizardite and chrysotile are present without antigorite, suggesting that deformation occurred along SSZs at $T < 300^\circ\text{C}$ (Evans, 2004). The formation of magnetite as a product of serpentinization places a lower T limit on serpentinization since Fe is more favorably incorporated into magnetite than serpentine at $T > 200^\circ\text{C}$ (Rouméjon et al., 2018). Therefore, serpentinization during STTFZ deformation can be roughly constrained to a T -window of 200°C – 300°C .

5.1.2. Fluid Availability During Serpentinization and Deformation

Serpentinization in the STTFZ is pervasive and occurred in an ocean-floor setting (Gass et al., 1994; MacLeod & Murton, 1993, 1995; Murton, 1986a) demonstrating that fluids, likely seawater, were readily available throughout the lithospheric mantle section that is now exposed in the Troodos Ophiolite. Because lizardite is thought to form from near-stoichiometric water:rock ratios (e.g., Viti & Mellini, 1998), the lizardite mesh microstructures observed suggest water:rock ratios were therefore likely to have been relatively low during the first phase of serpentinization. Chrysotile, which dominates slickenfibres, veins and some deformed serpentinites in the STTFZ (Figures 4c, 4d, and 7), is most commonly formed by the recrystallization of preexisting serpentine minerals where water:rock ratios are high (e.g., Andreani et al., 2005; Mumpton & Thompson, 1975; O'Hanley, 1991; O'Hanley et al., 1989). Therefore, the transition from lizardite to chrysotile in phyllonitic serpentinites (Figure 7) can be interpreted as a marker of locally elevated water:rock ratios (e.g., Evans, 2004; Rouméjon et al., 2015). Such elevation of water:rock ratios is likely to reflect locally enhanced fluid flow, because chrysotile preferentially occurs along localized shear zones where porosity and permeability are also elevated. Similar processes have been suggested for serpentinites in the San Andreas Fault (Moore et al., 1996).

5.1.3. Serpentinite Chemistry

The major element compositions of mesh rims, mesh cores, bastites, chrysotile in phyllonites, and antigorite and lizardite clasts within scaly and phyllonitic serpentinites are similar within each microstructurally defined group (Figure 9). Mesh rims and mesh cores contrast with bastite compositions, which are taken as representing the initial compositions of olivine and orthopyroxene, respectively. We find that chrysotile slickenfibres and phyllonitic shear fabrics have distinct and more homogeneous chemistry compared to lizardite in mesh microstructures, an observation that is consistent with higher water:rock ratios in the most

deformed serpentinites (e.g., Rouméjon et al., 2015). This is a consequence of the higher mobility of major elements, which would homogenize the composition of individual grains. The co-precipitation of magnetite with chrysotile is a possible explanation for the loss of Fe in the chrysotile compared with lizardite. Because mineralogical and chemical variability correlates well with distinct microstructures (Figure 9) within the STTFZ, we deduce that serpentinization was ongoing, and occurred in progressive stages under slightly different conditions as serpentinization became more localized with increasing strain. The preservation of this chemical variability argues against these fabrics having experienced any substantial reserpentinization subsequent to transform deformation, as a late-stage, post ocean-floor fluid influx and serpentinization event (e.g., Neogene emplacement-related uplift and weathering; MacLeod and Murton, 1993 and Gass et al., 1994) would be expected to overprint and homogenize their chemical and mineralogical differences (e.g., Nuriel et al., 2009).

5.1.4. Comparison Between the Southern Troodos Transform Fault Zone and Active Oceanic Transform Faults

Serpentine deformation was the predominant mode of deformation in the mantle lithosphere within the STTFZ and clearly exerted the primary control on the rheological behavior of the active transform plate boundary. The deformation model we propose is likely to be widely applicable to many, if not most, oceanic transform faults.

Our observations from Troodos require that seafloor serpentinization in the active domain of the transform was rapid and highly efficient, related to high fracture permeability and seawater influx deep into the mantle lithosphere. Such serpentinization, resulting in well-interconnected serpentine, occurs wherever mantle rocks are in contact with water at temperatures within the serpentine stability field. In many cases in the STTFZ, serpentinization demonstrably predated synkinematic “transform sequence” ultramafic and mafic magmatism (e.g., Figures 1b and 2; Gass et al., 1994; MacLeod & Murton, 1993; Murton, 1986a). Hydrothermal cooling and alteration is also common along active oceanic transforms, including recent evidence from the Blanco (Kuna et al., 2019) and Shaka and Prince Edward (Prigent et al., 2020) transform faults. In addition, the mafic crust at oceanic transforms is believed to be reduced in thickness relative to a “Penrose-type” layer-cake igneous crust (e.g., Auzende et al., 1989), either from reduced melt supply (e.g., Cannat, 1993; Cannat et al., 1995) or tectonic thinning (e.g., Fox & Gallo, 1984; Karson & Dick, 1983). Even at some intermediate- and fast-spreading settings (e.g., the Garrett transform on the East Pacific Rise; Hekinian et al., 1992) serpentinized mantle is exposed on the seafloor within the transform-tectonized domain, and therefore, it is reasonable to assume that our serpentine deformation model could be applicable in these cases too.

Insight into seafloor serpentinization may also be gained from extensional oceanic fault systems. Microseismicity suggests fluid flow from the sea floor to at least 12 km depth along the Mid Atlantic Ridge (Parnell-Turner et al., 2017) and 17 km at the South West Indian Ridge (Grevemeyer et al., 2019). This fluid flow is associated with greenschist facies phyllosilicate growth and deformation at the bases of detachment faults (Escartín et al., 2003; MacLeod et al., 2002). By analogy with these extensional faults at mid-ocean ridges, we predict serpentinization and serpentine deformation is likely to be typical of the shallow lithosphere of most transform faults. Note also that the strength of partially serpentinized peridotites drops to that of serpentine at only ~10%–15% alteration (Escartín et al., 2001). Therefore, the principle of hydration state and fabric development governing deformation of the lithospheric mantle in an oceanic transform fault is likely to be applicable in any location where serpentinization is an important process – that is, where fluids are introduced to the transform fault in mantle rocks within the serpentine stability field.

In our observations, lizardite and chrysotile are the stable serpentine phases, and this is typically the case at relatively shallow depth and low temperature ($T < 400^{\circ}\text{C}$; Evans, 2004), hence serpentine rheology should be widely appropriate for any hydrated lithospheric mantle where $T < 400^{\circ}\text{C}$. In the STTFZ, there is little evidence for antigorite, implying the rocks deformed at $<400^{\circ}\text{C}$, and this may be common in the near-transform mantle because of hydrothermal cooling (e.g., Roland et al., 2010). However, if temperatures of serpentinization were higher than in the rocks we observe, antigorite may occur instead of lizardite. The specific rheological differences between these polytypes are unclear, but antigorite has also been inferred to

be weak (Hilairt et al., 2007) and velocity-strengthening (Chernak & Hirth, 2010) at $T < 600^{\circ}\text{C}$ from laboratory constraints. Therefore, antigorite could still account for SSZ weakness, albeit deforming by different mechanisms.

5.2. Fabric Development of Serpentinite Shear Zones With Progressive Shear Strain

On the basis of our observations we find that macroscale fabrics in SSZs evolve from massive through scaly to phyllonitic with an inferred increase in bulk strain. This macroscale fabric evolution is accompanied by an evolution in microstructure from a mesh to a ribbon to a fibrous microstructure. Each microstructure is characterized by a distinct mineral composition, polytype and a dominant deformation mechanism (summarized in Figure 10). We deduce that the deformation mechanisms represented by each successive macroscale fabric and microstructure constrain the rheology of the serpentinized lithospheric mantle during transform-related deformation.

5.2.1. Evolution from Massive to Incipient Scaly Serpentinite

From our macroscopic observations we deduce that progressive development from massive (or fractured) serpentinite to an incipient scaly fabric is controlled by the formation and intersection of two fracture sets that accommodate shear displacement. These fractures are filled with fibrous chrysotile and isolate low strain angular, rhomboidal serpentinite blocks (Figure 3iii). The rhomboidal blocks (phacoids) retain the same low-strain mesh microstructure as in massive serpentinite, however, locally some blocks contain a ribbon texture, reflecting incipient ductile strain. In places, fractures with orientations and kinematics distinct from the phacoid-bounding shears and the STTFZ margins are observed, and can be explained as Riedel shears or as accommodating local rotation of more rigid blocks within the broad STTFZ (MacLeod & Murton, 1993, 1995).

5.2.2. Evolution From Incipient Scaly Serpentinite to a Scaly Fabric

With progressive transform displacement rhomboidal blocks defining the incipient scaly fabric develop into smaller sigmoidal phacoids with higher aspect ratios (Figure 3iii). Scaly serpentinite phacoids have asymmetry indicating bulk dextral slip subparallel to the STTFZ margin (Figure 4b). Compared to their cores, phacoid margins may have greater concentrations of magnetite or fibrous chrysotile (Figures 10b and S3b). These mineralogical variations are inferred to reflect, respectively, local dissolution of serpentine, enhancing the concentration of relatively insoluble magnetite, and local dilation providing space for the precipitation of fibrous chrysotile as shear vein coatings. Dissolution-precipitation processes are therefore important in the progressive development of scaly serpentinite fabrics, as also suggested by Vannucchi et al. (2003) and Schleicher et al. (2012).

The low-strain mesh microstructure common in massive serpentinite is replaced by a pervasive ribbon microstructure in scaly serpentinite. During this transition mesh cores become smaller but progressively more elongated with increasing bulk strain, with their long axes parallel to the long axis of the strain ellipsoid. The transition from mesh to ribbon microstructure is controlled by mesh rims deforming differently depending on their orientation relative to the maximum principal compressive stress (σ_1). When sheared, they can respond in two ways: either they maintain a favorable angle between their (001) plane and the kinematic XY plane, or else they rotate, becoming unfavorably oriented to the shear direction (Viti et al., 2018). Favorably oriented rims, subparallel to the XY plane (45° to σ_1), experience maximum shear stress and form anastomosing 3D networks of aligned lizardite that define a foliated, anisotropic ribbon microstructure. Once formed, a ribbon microstructure comprises a strong shape preferred orientation (SPO) in aligned lizardite grains, defining a foliation, and where deformation can be controlled by easy basal (001) glide (Figures 10e and 10f) (e.g., Viti et al., 2018) because of lizardite's simple structure and slip systems (e.g., Amiguet et al., 2014; Hilairt et al., 2007; Hirauchi et al., 2010; Viti et al., 2018). In contrast, unfavorably oriented rims experience higher normal stresses, and favor deformation by pressure solution (Viti et al., 2018), rather than undergoing deformation by dislocation creep or kinking. This microstructural transition, largely controlled by dissolution, allows the concentration of insoluble magnetite around ribbon cells, forming seams traceable up to a few millimeters (Figure 6b). These magnetite-rich seams have the potential to influence local rheology since magnetite is strong and brittle compared to serpentine. This may promote unstable slip, as suggested by Tarling et al. (2018).

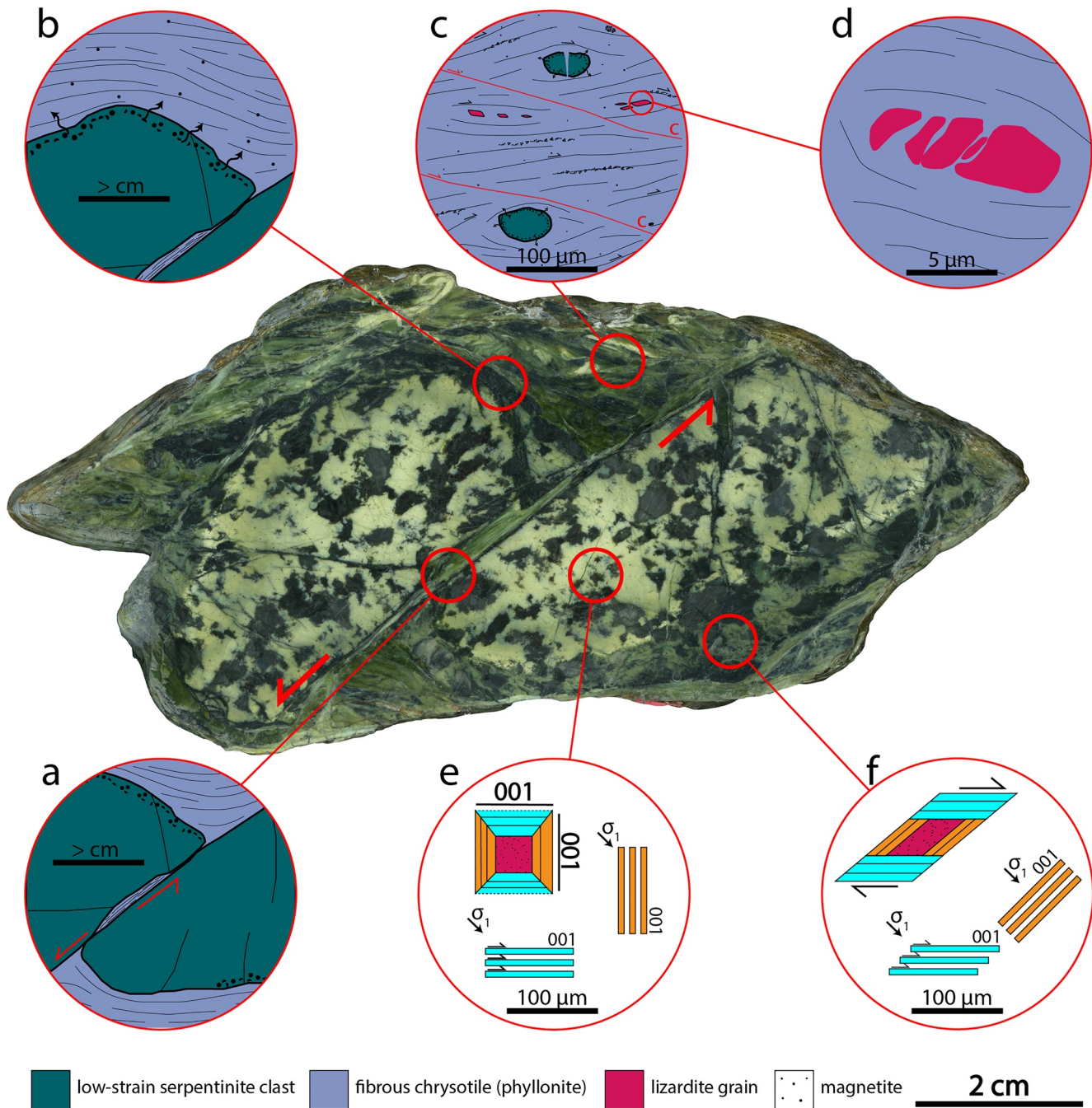


Figure 10. Microstructural summary of deformation within Southern Troodos Transform Fault Zone serpentinites. (a) Brittle fracture of massive serpentine blocks increasing permeability and fluid flow, and precipitation of chrysotile fibers. (b) Dissolution at the edges of serpentine blocks, concentrating magnetite. (c) Scaly to phyllonitic fabric defining an S-C geometry and accommodating deformation by fiber-on-fiber slip between well-aligned fibers of chrysotile. (d) Breakdown of relict lizardite grains by fracturing and dissolution to precipitate chrysotile. (e) Low strain mesh microstructure toward the core of blocks that deforms at the edges to a ribbon microstructure (f) following shearing. This transition is accommodated by a combination of rotation of mesh rims, pressure solution and (001) glide.

5.2.3. Evolution From Scaly to Phyllonitic Serpentine

Phyllonitic fabrics characterize the most highly strained serpentinites exposed in the STTFZ. The progression from scaly fabric to phyllonitic fabric involves low-strain phacoids in scaly serpentine becoming progressively smaller and volumetrically less significant. In addition, the chrysotile component of serpentine

becomes increasingly dominant over lizardite. As a consequence of the reduction in phacoid size, cleavage becomes more planar (Figures 4b and 4e). Chrysotile fibers form an interconnecting network with a strong SPO reflecting bulk shear zone kinematics (Figure 6c) and surround isolated low-strain phacoids that internally preserve a mesh to ribbon microstructure. This observation is comparable to other examples of SSZs (e.g., Andreani et al., 2005; Collettini et al., 2011; Collettini et al., 2009; Hirauchi & Yamaguchi, 2007; Smith et al., 2011; Wicks & Whittaker, 1977).

In the phyllonitic serpentinite, chrysotile fills fractures in relict lizardite grains (Figure 7a), suggesting lizardite deformed brittlely, at least locally, and was actively replaced by chrysotile during transform-related shearing. This is supported by the observation that lizardite grains are aligned to the foliation but not present in strain shadows. The formation of chrysotile by dissolution of lizardite should be particularly efficient in areas characterized by low strain rates and fine grain size (e.g., Rutter, 1976).

A strong SPO in chrysotile in phyllonitic serpentinite has been previously explained by two processes (Andreani et al., 2005; Reinen, 2000): (1) mechanical, rigid-body rotation of preexisting chrysotile fibers controlled by the finite extension direction, and/or (2) the synkinematic growth of newly precipitated chrysotile controlled by the local opening direction. The aligned fibrous chrysotile grains in phyllonitic serpentinite contrasts in shape to the shorter, more equant lizardite grains and ultra-fine chrysotile that make up mesh rims and cores (Figure S3). This supports the deduction that the chrysotile in phyllonitic serpentinite grew synkinematically, subparallel to the shear direction, rather than by the reorientation of preexisting chrysotile. Dissolution-precipitation has been proposed as a mechanism for synkinematic growth, at low strain rates and temperatures up to $\sim 450^{\circ}\text{C}$, for forming phyllonitic serpentinite within several other serpentinite-bearing fault zones (e.g., Padrón-Navarta et al., 2012; Wassmann et al., 2011) including the Santa Ynez Fault along the San Andreas fault system (e.g., Andreani et al., 2005). Dissolution-precipitation processes are inferred to be the low- T equivalent of dynamic recrystallization for serpentine (e.g., Amiguet et al., 2014) and is the operative process in the STTFZ because the temperatures were too cold for efficient dislocation creep in lizardite.

Where the phyllonitic serpentinite fabric is well-developed, most of the original mesh and ribbon microstructure has been replaced by chrysotile fibers. The strong SPO and 3D interconnectivity of chrysotile domains promotes fiber-on-fiber slip as a deformation mechanism (Viti et al., 2018) (Figure 10c) because of chrysotile's low frictional strength ($\mu \sim 0.15$; Tesei et al., 2018). Chrysotile fibers are commonly bent or curved, as resolved from undulose extinction, suggesting some deformation is taken up by the ease of bending rather than dislocation creep as a bulk deformation mechanism.

5.2.4. Brittle Deformation in Serpentinite Shear Zones

While we infer that most of the preserved fabrics formed by dissolution-precipitation following the formation of a relatively small-displacement fracture fabric, brittle deformation features have mutually cross-cutting relationships with all the dominant macroscale ductile fabrics (Figures 2, 3 and 5). Macroscopically, discrete fault planes are observed adjacent and parallel to block margins (Figures 5a and 5b). This observation is significant because it implies that steep gradients in strain and strain rates expected at the boundaries between foliated matrix and low-strain blocks promote brittle fracturing (e.g., Fagereng & Sibson, 2010; Kenkmann & Dresen, 1998), in a similar way to that modeled by Beall et al. (2019). Macro- and microscale S-C geometries (Figures 4b, 5 and 6c) within SSZs highlight the coeval brittle-ductile deformation across all scales, with dissolution common along curved foliation planes, and localized displacement on more planar C planes (Figure 10c). These competing frictional-viscous deformation processes and S-C geometries are directly comparable to observations from other scaly fault zones (e.g., Vannucchi et al., 2003). Fracturing as a mechanical means of breaking down serpentinite blocks and phacoids in scaly and phyllonitic serpentinites is also common (Figures 4b and 10a), as a result of block interaction accommodating bulk rotation during shearing. Brittle deformation is an important mechanism allowing localized and elevated water:rock ratios in shear zones to promote the dissolution-precipitation mechanisms, the precipitation of chrysotile and foliation development.

5.2.5. Summary of the Progressive Deformation and Evolution of Serpentinite Shear Zones

In summary, we document a progressive development from (1) isotropic lizardite-rich mesh microstructure through (2) lizardite-rich ribbon microstructure in low-strain, scaly serpentinite with local chrysotile precipitated around phacoids, to (3) a fibrous chrysotile phyllonite with a well-developed foliation. These transitions can be inferred to represent a bulk strain progression, and may also reflect a temporal evolution within an individual SSZ within the broader active transform fault zone. However, bulk strain within the STTFZ is not homogeneously distributed; rather, deformation is partitioned into anastomosing SSZs which are themselves composed of multiple zones of the different fabric types discussed above. These zones of different fabric types have composite thicknesses ranging from cm to several hundreds of m, each reflecting different amounts of accumulated strain. It is important to emphasize that total strains accumulated on individual SSZs are accommodated by all fabric types combined and most likely simultaneously.

5.3. Are Serpentinite Shear Zones Weak?

Previous studies have considered how the deformation of serpentinite affects the rheology and seismic behavior of oceanic transform faults from dredged samples (e.g., Kohli & Warren, 2020; Prigent et al., 2020; Warren & Hirth, 2006) and exhumed mantle on the Bogota Peninsula, New Caledonia (e.g., Chatzaras et al., 2020). Chatzaras et al. (2020) discuss the contribution of stress changes imposed following a downward propagation of a seismic rupture from the crust into the mantle. They discuss the change in deformation mechanism from brittle fracture during the coseismic period to dynamic crystallization at the postseismic stage of the earthquake cycle at temperatures $>820^{\circ}\text{C}$. Kohli and Warren (2020) and Prigent et al. (2020) considered deformation at $\sim 500^{\circ}\text{C}$ – 875°C and depths of 20–25 km recorded in samples dredged from the Shaka and Prince Edward oceanic transforms, documenting brittle and ductile deformation of mylonites. These studies conclude that fluid-rock interaction promotes the crystallization of weak mineral phases and grain size reduction, which in turn provide mechanisms that can account for fault weakening and strain localization, including dissolution-precipitation, as we suggest is also important at lower T ($<300^{\circ}\text{C}$).

The studies of dredged and exhumed mylonites document higher-temperature brittle deformation than expected for the base of the thermally controlled seismogenic zone ($>600^{\circ}\text{C}$ isotherm) but do explain geophysical observations (e.g., Kuna et al., 2019; McGuire et al., 2012; Roland et al., 2010; Wolfson-Schwehr et al., 2014) of seismicity locally extending much deeper (e.g., down to 25 km; Prigent et al., 2020) and therefore to temperatures approaching $1,000^{\circ}\text{C}$ (e.g., Froment et al., 2014; McGuire et al., 2012; Wolfson-Schwehr et al., 2014). A consequence of this observation is that fractures may allow fluids to flow into the dominantly viscous mantle below the seismogenic layer, inducing fluid-related weakening mechanisms and strain localization (Kohli & Warren, 2020). Therefore, whilst in the STTFZ we are not able to characterize deformation corresponding to such depths or temperatures, relict high- T mylonites (e.g., Figure 4a) previously documented in the lithospheric mantle of the STTFZ almost certainly correspond to an earlier higher-temperature, preserpentinization deformation episode for which limited evidence has been documented by Murton (1986a), MacLeod and Murton (1993), Gass et al. (1994), and Fagereng and MacLeod (2019) within the STTFZ mantle section.

It is very clear that serpentine, not olivine, controlled the lithospheric mantle rheology in the STTFZ during the active strike-slip plate boundary phase of deformation. It is evident that the overall structure and composition of SSZs within the STTFZ represents deformation within well-hydrated, pervasively serpentinized lithospheric mantle along oceanic transform faults active at $T < 300^{\circ}\text{C}$. Because serpentinites in the STTFZ contain a range of microstructures and different serpentine polymorphs, the strength of the serpentinites may vary in space and time as a function of deformation mechanism and serpentine polytype. On the basis of deformation experiments extrapolated to geological strain rates, elevated pressures (>200 – 300 MPa) and temperatures ($>300^{\circ}\text{C}$) we can deduce that lizardite and chrysotile are weak phases. Both lizardite and chrysotile have frictional strengths, μ , of ~ 0.2 from room temperature up to $\sim 200^{\circ}\text{C}$ and effective normal stresses of 5–120 MPa, that is, conditions consistent with those in the brittle upper lithosphere (Tesei et al., 2018). Chrysotile can have a μ as low as 0.1 at shallow burial depths, <3 km (Moore et al., 1997). In contrast to individual serpentine polytypes, mesh microstructures have stronger frictional strengths, $\mu \approx 0.3$ under the same conditions (Tesei et al., 2018), and remain weak at elevated temperatures (Viti et al., 2018)

and pressures up to 400 MPa (Escartín et al., 1997). Therefore, the frictional weakness of serpentine polytypes and microstructure is likely to play a role in SSZ weakness.

From our observations we document not only a strain-progressive change in serpentine polytype, from lizardite to chrysotile, that would explain minor weakening ($\Delta\mu \leq 0.1$), but also a change in the microstructure from mesh to ribbon and phyllonitic serpentinite. The ease of (001) plane sliding in lizardite is expected to be similar to that of micas, where glide is easiest when the basal plane is oriented at $\leq 45^\circ$ to the axis of greatest compression (Kronenberg et al., 1990) such that, when (001) crystallographic planes rotate toward the shear plane with increasing strain (Figure 10e; Section 5.3.2), the lizardite basal planes form a mechanically weak foliation.

We deduce that weakening of the SSZs is likely to have occurred by ongoing dissolution-precipitation processes coupled to frictional sliding (e.g., Bos & Spiers, 2002; Tesi et al., 2018). Macroscopically, fractures and cleavage planes in scaly serpentinites are highly anastomosing, which would limit the ease of frictional sliding of phacoids. However, with increased shearing, phacoid sizes and proportions are reduced and at least partially replaced with fibrous chrysotile, a process aided by dissolution-precipitation. It is well accepted that the interconnectivity of the weak phase is important in controlling bulk shear zone rheology (Handy, 1990). Therefore, as the volume proportion of fibrous chrysotile increases, the volume and interconnectivity of the weak phase increases bulk weakening of the SSZs.

Our evidence from the STTFZ suggests that the frictional strength of individual SSZs decreases with cumulative shear strain when high porosity, permeability and pervasive fluid flow promotes the formation of foliated serpentinite (ribbon or phyllonitic microstructure). Foliation development acts as an efficient weakening mechanism in low- and high-strain serpentinites, providing a mechanism of strain localization that may be active along many oceanic transform faults in the shallow (serpentinized) lithospheric mantle at temperatures $\sim 300^\circ\text{C}$. This is similar to the long-term weakening of continental transforms that is suggested to occur following the development of chlorite or muscovite phyllonites by a broadly comparable process (Holdsworth et al., 2001; Imber et al., 1997). As well, our model suggests that the development of a well-interconnected, well-foliated serpentinite implies high fluid pressures are not required to generate the low fault strength that is often inferred for oceanic transforms (e.g., Angelier et al., 2000; Homberg et al., 2010).

The relative internal proportion and distribution of serpentinite fabrics within shear zones is important. Strain accumulation is heterogeneous (Figure 5; Section 5.2) and therefore strength will also be spatially (and temporally) heterogeneous. Areas that did not experience serpentinization early during deformation, or retain a low-strain mesh microstructure, have the potential to act as strong asperities within weak, foliated SSZs (e.g., Figure 5).

5.4. Seismic Style of Serpentinite Shear Zones

At the macroscale, bulk deformation occurred in a distributed, ductile manner within scaly and phyllonitic serpentinites. This style of distributed deformation is similar to that thought to accommodate steady creep at low shear stresses in serpentinite along the San Andreas Fault (e.g., Andreani et al., 2005; Irwin & Barnes, 1975; Moore & Rymer, 2007).

At slow slip rates ($\sim 10^{-9}$ m/s) serpentinites deformed in laboratory experiments are generally weak and display velocity-strengthening behavior (Andreani et al., 2005; Kohli et al., 2011; Moore et al., 1997; Moore et al., 1996; Reinen et al., 1994). However, it is suggested that velocity-weakening, seismogenic behavior can occur in lizardite-rich serpentinites in response to elevated slip rates (~ 0.1 m/s; Kohli et al. (2011)), potentially induced by processes such as: (1) earthquake nucleation elsewhere; (2) local or temporal stress concentrations; (3) shear strength decrease due to increased fluid pressure; (4) changes to the thickness of the deforming zone (Reinen et al., 1991, 1994); and/or (5) increased temperature by shear heating (Hirth & Guillot, 2013; Moore et al., 1997; Moore et al., 2004). In contrast to lizardite, however, chrysotile exhibits a velocity-independent behavior, remaining velocity-strengthening at all laboratory strain rates under hydrothermal conditions (Moore et al., 1997; Moore et al., 1996; Reinen, 2000). This is significant, as it suggests chrysotile-rich phyllonitic serpentinites, such as those we document in the exhumed STTFZ, are likely to favor stable creep under all conditions.

Scaly fabrics similar to those documented here from the STTFZ can be found in various tectonic settings and mineral assemblages, and are often associated with the whole spectrum of slip speeds, from creep (Vannucchi et al., 2003) to earthquake rupture propagation (e.g., during the 2011 M9 Tohoku-Oki earthquake; Chester et al., 2013). This contrasts with the occurrence of discrete C planes throughout scaly serpentinite outcrops that partly retain lizardite-rich mesh and ribbon microstructures. We suspect, therefore, that discrete deformation structures, such as throughgoing fault planes (e.g., Figures 4b and 4f), in the STTFZ developed where slip velocities were most easily elevated spatially (locally) or temporally. Principal slip zones are likely necessary for seismic slip (Ikari, 2015), but have not been observed within the serpentine phyllonites we describe here. The phyllonites can therefore be interpreted as favoring aseismic shear, although we cannot exclude the possibility of transient seismic slip, nucleating elsewhere but propagating along discrete surfaces that were not preserved (see also Section 5.5 below).

Most of the brittle fractures preserved are those defining low-strain serpentinite phacoids, with traced lengths on the order of tens of cm. The size of a fracture plays a role in the moment magnitude, M_w , of an earthquake generated by slip along that fracture (Hanks & Kanamori, 1979). M_w is proportional to log of the moment, M_0 , which is defined as a scalar by the rupture area (A) * average slip (d) * shear modulus of surrounding rock (G) (Aki, 1966). Following scaling relations by Kanamori and Anderson (1975), circular ruptures with diameter ~ 10 cm (i.e., on the same order of magnitude as the fractures in scaly serpentinite) will produce M_w of ~ -1 , if displacement is caused by a single event (G of serpentinite = 20 GPa; Reynard et al., 2007). Seismicity of $M_w > 0$ (reflecting faults with ~ 30 cm radius, still within the range of fractures within scaly serpentinite), has been documented along several active oceanic transform faults such as the Gofar (e.g., Froment et al., 2014; McGuire et al., 2012), Blanco (e.g., Kuna et al., 2019) and Discovery faults (e.g., Wolfson-Schwehr et al., 2014) in the course of highly detailed ocean bottom seismometer surveys. However, whilst individual fractures in scaly serpentinite are small, it is likely that deformation is accomplished by localized slip along C planes, or on numerous fractures that interact and link up to accommodate greater overall displacements and magnitudes than calculated above.

SSZs in the STTFZ are internally variable in their deformation style, with zones of dominantly brittle deformation, mixed brittle-ductile deformation and ductile deformation (Figure 5). They contrast with many other mélanges from other geological environments in that most of the blocks and matrix are derived from the same protolith, so ultimately the strength contrast within SSZs has to come from a strain weakening mechanism. In the case of the STTFZ we have shown here that this occurred through the development of a foliation from an initial isotropic mesh microstructure, accompanied by reactions replacing lizardite with chrysotile, and grain size reduction (Section 5.3). Areas that are dominated by massive serpentinite and display discrete faults could therefore act as asperities (Figure 11), whilst areas that are dominated by well-interconnected scaly or phyllonitic fabric are more likely representative of weak serpentinite. Where phacoid proportions are high, and scaly or phyllonitic matrix is poorly interconnected (Figure 5a), discrete throughgoing fractures are widespread, potentially reflecting locally elevated strain rates (Fagereng & Sibson, 2010). Those portions of SSZs dominated by well-interconnected scaly to phyllonitic serpentinite, on the other hand, predominately record distributed deformation, and most likely acted as a creeping matrix at the macroscale (Figure 5c).

The structure and rheology of the lithospheric mantle must evolve as a function of time, strain and serpentinization (therefore, as a function of permeability and fluid flux), much like inferred for the Shaka and Prince Edward oceanic transforms (Prigent et al., 2020). On the basis of our observations, mixed, low temperature brittle-ductile deformation occurs pervasively throughout SSZs, with coeval structures. Some of these structures may record seismicity, but others are likely to have been aseismic (Figure 11), under temperatures far less than the inferred thermally controlled base of the seismogenic zone at $\sim 600^\circ\text{C}$ (e.g., Abercrombie & Ekström, 2001; Braunmiller & Nábělek, 2008). These different deformation styles can occur simultaneously where fracturing and dissolution-precipitation processes compete, or may alternate between one another where increased slip rate allows brittle fracture of an otherwise creeping serpentinite. This is analogous to, and provides a rheological framework for, a “multimode” conceptual model for the behavior of the serpentinized lithospheric mantle within oceanic transform faults (e.g., Boettcher & Jordan, 2004), which proposes individual fault segments can undergo both seismic and aseismic slip at different times. This is also similar to the model presented by Kuna et al. (2019), who suggested that the lithospheric mantle part of the Blanco transform fault undergoes seismic and aseismic slip at different times.

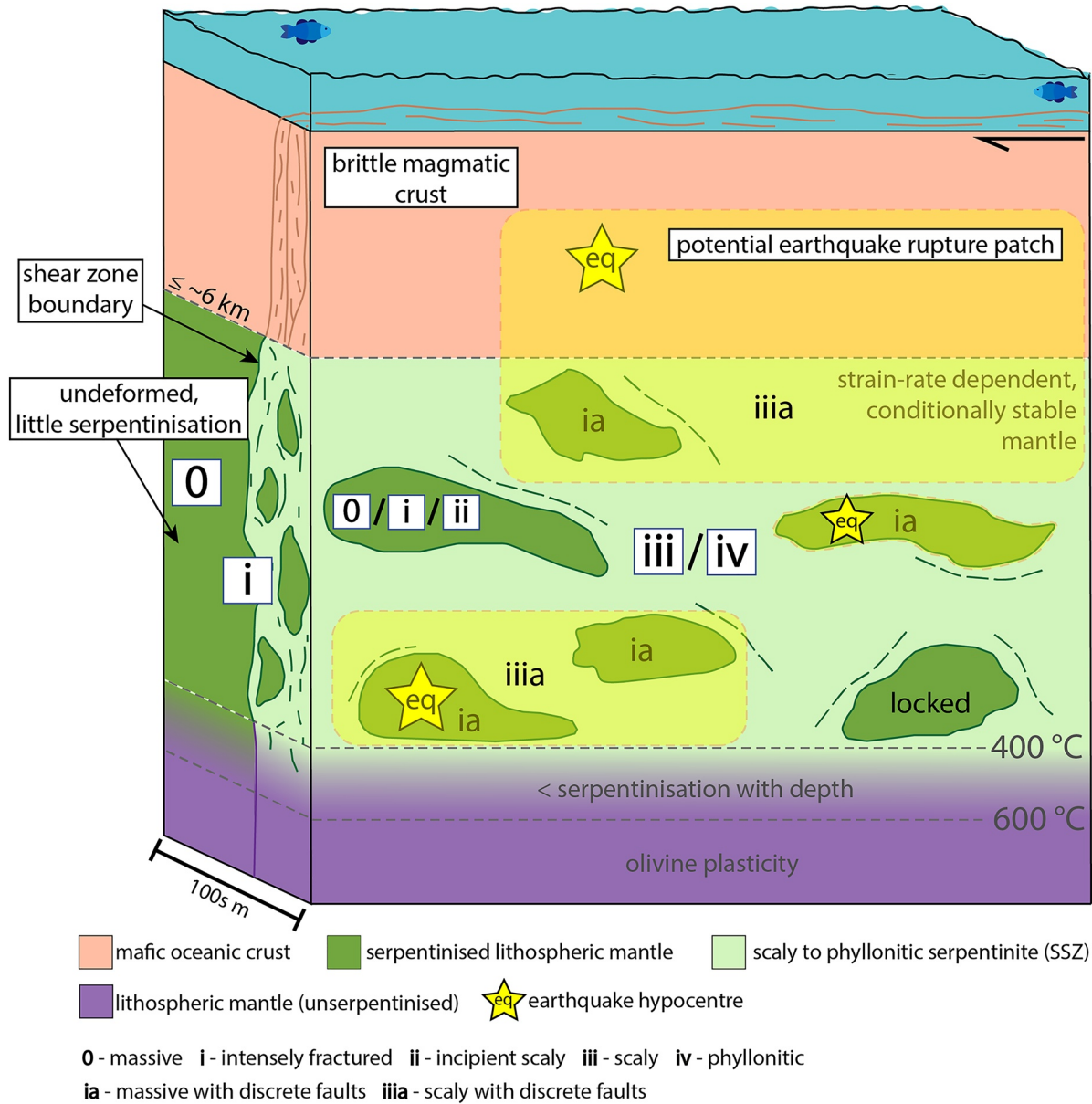


Figure 11. Schematic summary of the deformation and mode of slip along an oceanic transform fault based on observations from the mantle lithosphere of the Southern Troodos Transform Fault Zone. Crustal thickness of ≤ 6 km shown is a simplified, approximate maximum depth to the base of a magmatic crustal layer, while the depths to the 400 and 600°C isotherms would depend on a range of factors including the geothermal gradient, spreading rate, magmatic crustal thickness and fluid infiltration. Pervasively serpentinized lithospheric mantle transitions progressively through scaly to phyllonitic serpentinite (0–iv; as in Figure 3) with continued deformation, and is accompanied by a transition from microseismicity to aseismic creep at $T < 600^\circ\text{C}$. Preserved mesh-textured serpentinite areas (darker green) may represent parts of the lithospheric mantle that were not well serpentinized during deformation, and hence act as locked patches where earthquakes can nucleate, and allow the propagation of an earthquake (yellow patch), as a result of loading from the otherwise creeping lithospheric mantle. Similarly, an earthquake nucleating in the brittle mafic crust may be capable of propagating downward into the serpentinized lithospheric mantle, as a consequence of the conditionally stable nature of serpentine.

5.5. The Interaction Between Mantle Shear Zones and Crustal Faults

Many of the structures we document are intrinsic, having formed from local processes within individual SSZs. However, this does not rule out some features, particularly the larger throughgoing discrete faults, having been imposed from elsewhere, formed from the propagation of a coseismic rupture that nucleated in a potentially distant asperity, for example in the mafic oceanic crust (Figure 11). This raises the important question of how the crust and mantle are coupled along oceanic transform faults. Brittle faults could

nucleate in the mafic crust, perhaps as a result of being loaded by the creeping serpentinitized lithospheric mantle below, and propagate downwards into the lithospheric mantle, as suggested for the Romanche (Ab-ercrombie & Ekström, 2001) and Blanco transform faults (Kuna et al., 2019), introducing fluids and promoting serpentinitization. Alternatively, creeping SSZs within the serpentinitized lithospheric mantle could load adjacent undeformed serpentinite, comprising a mesh microstructure that creeps at a slower rate, explaining how seismic slip can occur within the serpentinitized lithospheric mantle (Figure 11). Earthquakes that nucleate in massive serpentinite, loaded by surrounding creeping SSZs, may also propagate back up into the mafic crust. Because the fluids responsible for hydration to serpentinite are seawater and percolate down into the lithospheric mantle, it is consistent with the idea that SSZs are generally the down dip continuation of crustal faults.

It is important to recognize that the well-documented, multi-scale geological complexity of the Southern Troodos Transform Fault Zone is almost certainly mirrored by modern oceanic transform fault zones, although their details can only be hinted at. Along many slow- and ultraslow spreading ridges a regular, continuous magmatic oceanic crust is now known to be absent or incompletely developed, especially near ridge axial discontinuities, and the interplay between magmatism and tectonic extension is complex (e.g., Cannat, 1993; Cannat et al., 1995; Cann et al., 1997; Karson et al., 2006). Even within the STTFZ in the Troodos ophiolite where, at the ridge axis, a continuous Penrose-type mafic ocean crust was generated, detailed field mapping of the transform-tectonized domain has documented substantial vertical, oblique and rotational displacements on many transform-related fault zones, consequently juxtaposing crust and mantle lithologies on a range of scales adjacent to and within the active transform-tectonized zone (Gass et al., 1994; MacLeod, 1990; MacLeod et al., 1990; MacLeod & Murton, 1993, 1995; Murton, 1986a). Furthermore, magmatic intrusions, documented in the STTFZ (into already serpentinitized mantle: Gass et al., 1994; MacLeod & Murton, 1993; Murton, 1986a, 1986b) and also some modern transforms (e.g., Constantin, 1999), can influence the local P-T conditions and induce metasomatic reactions that affect local rheology (e.g., Tarling et al., 2019). Variation in fluid flow and associated serpentinitization will also influence the seismic behavior due to the heterogeneous distribution of frictionally weak, hydrous minerals (e.g., Boettcher & Jordan, 2004; Moore et al., 1997) and heterogeneous fluid pressures (e.g., Scholz, 1998). Therefore, there are circumstances where different and additional mechanisms are likely to operate at a variety of spatial and temporal scales.

6. Conclusions

The Southern Troodos Transform Fault Zone (STTFZ) records sub-seafloor faulting and deformation within a Tethyan oceanic transform fault. Subsequent exhumation has allowed us a unique insight into its 3D internal structure and geological evolution, and an examination of deformation mechanisms within the shallow lithospheric mantle that corresponds to the deeper part of the seismogenic zone in modern oceanic transform fault zones. We show that transform plate motion in the lithospheric mantle was accommodated almost exclusively by deformation of serpentinite. Steeply dipping, E-W striking (transform-parallel), serpentinite shear zones (SSZs) with strike-slip lineations document original seafloor deformation within a once dextrally slipping oceanic transform fault zone. Exhumation-related overprinting is absent or minor, and readily accounted for in selected exposures. Present-day outcrop of serpentinitized mantle peridotite preserves a record of variable deformation at the macro- and microscale. The dominant structures that accommodated deformation within the lithospheric mantle are shear zones comprising a serpentinite mélange within which the volumetric proportion of foliated serpentinite matrix increases with inferred cumulative strain. Individual SSZs are of the order of tens–100 m wide, with anastomosing geometries, and can be traced for up to several kilometers along strike, within an overall transform-tectonized zone ~5 km wide.

Massive serpentinite has a mesh texture at the microscale, resulting from passive influx of water into the olivine lattice. This microstructure is pervasive within the overall STTFZ and implies extensive seawater penetration from above along both transform- and ridge-parallel faults. From a detailed examination of the internal structure of SSZs within the transform-tectonized zone as a whole, we find a progressive transition from massive serpentinite to scaly and phyllonitic serpentinite at the macroscale. This is matched by a textural change from mesh to ribbon and fibrous microstructures, along with a change in dominant serpentine type from lizardite to chrysotile. This scaly fabric experienced basal (001) glide and pressure solution to

form a foliated ribbon microstructure. In concert with this, dissolution-precipitation along fractures was responsible for the formation of a chrysotile-rich phyllonitic serpentinite at the expense of the lizardite-rich mesh and ribbon microstructures. Once foliated chrysotile serpentinite developed, fiber-on-fiber slip acted as an efficient weakening mechanism promoting stable creep. Brittle fracture of serpentinite occurred locally and is important, because the fractures promoted fluid flow, enhancing many of these deformation mechanisms without the need for elevated fluid pressures.

We have shown here that SSZs are mechanically weak because of the intrinsic nature of foliated lizardite and chrysotile, and that they deform largely by aseismic creep at geological strain rates and low temperatures (from 400°C down to seafloor temperature). SSZ strength decreases with the development of a foliation caused by progressive shearing. SSZs can, however, be capable of hosting coseismic slip if external factors allow an increase in slip rate, because this promotes velocity-weakening behavior in lizardite (Kohli et al., 2011). We argue that these observations and inferences can explain spatial and temporal variations in the rheology and seismic behavior of modern oceanic transforms. Seismically coupled segments may occur in regions where serpentinitization is less pervasive, or where zones retain an original mesh microstructure, and are therefore relatively strong. The rheological evolution of the oceanic lithosphere is therefore heterogeneous where it is controlled by the spatiotemporal variation in serpentinite fabric development, which in turn is controlled by heterogeneous fracturing, permeability and fluid flow. On the basis of evidence from the Southern Troodos Transform Fault Zone of Cyprus we deduce that the ‘seismic deficit’ and requirement for abundant aseismic creep in the shallow lithospheric mantle in oceanic transform faults is explained by the weak mechanical behavior of compound serpentinite shear zones, whose complex internal structures are capable of hosting spatially and temporally variable seismic behavior.

Data Availability Statement

Structural, SEM, and Raman data can be accessed at <http://doi.org/10.5281/zenodo.3982653>.

Acknowledgments

S. Cox is supported by a NERC GW4+ Doctoral Training Partnership studentship from the Natural Environment Research Council [NE/L002434/1]. A. Fagereng is supported by the European Research Council (ERC) Horizon 2020 Program (715836). Thanks to support from Director and staff of Cyprus Geological Survey Department. The authors thank Duncan Muir for assistance with scanning electron microscopy and Tony Oldroyd for sample preparation. The authors also extend our thanks to the Otago Raman Laboratory. Thanks to Chris Tulley for assistance in the field. The authors thank three anonymous reviewers for their constructive feedback, which improved this manuscript significantly. Open access funding enabled and organized by Projekt DEAL.

References

- Abercrombie, R. E., & Ekström, G. (2001). Earthquake slip on oceanic transform faults. *Nature*, 410(6824), 74–77. <https://doi.org/10.1038/35065064>
- Aki, K. (1966). Generation and propagation of G waves from the Niigata Earthquake of June 16, 1964. Part 2. Estimation of earthquake movement, released energy, and stress-strain drop from the G wave spectrum. *Bulletin of the Earthquake Research Institute, University of Tokyo*, 44(1), 73–88.
- Amiguet, E., Van De Moortèle, B., Cordier, P., Hilaret, N., & Reynard, B. (2014). Deformation mechanisms and rheology of serpentinites in experiments and in nature. *Journal of Geophysical Research: Solid Earth*, 119(6), 4640–4655. <https://doi.org/10.1002/2013JB010791>.SolidEarth
- Andreani, M., Boullier, A.-M., & Gratier, J.-P. (2005). Development of schistosity by dissolution-crystallization in a Californian serpentinite gouge. *Journal of Structural Geology*, 27(12), 2256–2267. <https://doi.org/10.1016/j.jsg.2005.08.004>
- Angelier, J., Bergerat, F., & Homberg, C. (2000). Variable coupling across weak oceanic transform fault: Flateyjarskagi, Iceland. *Terra Nova*, 12(3), 97–101. <https://doi.org/10.1046/j.1365-3121.2000.123279.x>
- Auzende, J.-M., Bideau, D., Bonatti, E., Cannat, M., Honnorez, J., Lagabrielle, Y., et al. (1989). Direct observation of a section through slow-spreading oceanic crust. *Nature*, 337(6209), 726–729. <https://doi.org/10.1038/337726a0>
- Beall, A., Fagereng, Å., & Ellis, S. (2019). Strength of strained two-phase mixtures: Application to rapid creep and stress amplification in subduction zone mélange. *Geophysical Research Letters*, 46(1), 169–178. <https://doi.org/10.1029/2018gl081252>
- Boettcher, M. S., Hirth, G., & Evans, B. (2007). Olivine friction at the base of oceanic seismogenic zones. *Journal of Geophysical Research*, 112(B1). <https://doi.org/10.1029/2006jb004301>
- Boettcher, M. S., & Jordan, T. H. (2004). Earthquake scaling relations for mid-ocean ridge transform faults. *Journal of Geophysical Research*, 109(B12). <https://doi.org/10.1029/2004jb003110>
- Bonhommet, N., Roperch, P., & Calza, F. (1988). Paleomagnetic arguments for block rotations along the Arakapas fault (Cyprus). *Geology*, 16(5), 422–425. [https://doi.org/10.1130/0091-7613\(1988\)016<0422:PAFBRA>2.3.CO;2](https://doi.org/10.1130/0091-7613(1988)016<0422:PAFBRA>2.3.CO;2)
- Bos, B., & Spiers, C. J. (2002). Frictional-viscous flow of phyllosilicate-bearing fault rock: Microphysical model and implications for crustal strength profiles. *Journal of Geophysical Research*, 107(B2), ECV 1-1–ECV 1-13. <https://doi.org/10.1029/2001JB000301>
- Braunmiller, J., & Nábělek, J. (2008). Segmentation of the blanco transform fault zone from earthquake analysis: Complex tectonics of an oceanic transform fault. *Journal of Geophysical Research*, 113(B7). <https://doi.org/10.1029/2007jb005213>
- Cann, J. R., Blackman, D. K., Smith, D. K., McAllister, E., Janssen, B., Mello, S., et al. (1997). Corrugated slip surfaces formed at ridge-transform intersections on the Mid-Atlantic Ridge. *Nature*, 385(6614), 329–332. <https://doi.org/10.1038/385329a0>
- Cannat, M. (1993). Emplacement of mantle rocks in the seafloor at mid-ocean ridges. *Journal of Geophysical Research*, 98(B3), 4163–4172. <https://doi.org/10.1029/92jb02221>
- Cannat, M., Mevel, C., Maia, M., Deplus, C., Durand, C., Gente, P., et al. (1995). Thin crust, ultramafic exposures, and rugged faulting patterns at the Mid-Atlantic Ridge (22°–24°N). *Geology*, 23(1), 49–52. [https://doi.org/10.1130/0091-7613\(1995\)023<0049:Tcuar>2.3.Co;2](https://doi.org/10.1130/0091-7613(1995)023<0049:Tcuar>2.3.Co;2)
- Ceuleneer, G., Nicolas, A., & Boudier, F. (1988). Mantle flow patterns at an oceanic spreading centre: The Oman peridotites record. *Tectonophysics*, 151(1–4), 1–26. [https://doi.org/10.1016/0040-1951\(88\)90238-7](https://doi.org/10.1016/0040-1951(88)90238-7)

- Chatzaras, V., Tikoff, B., Kruckenberg, S. C., Titus, S. J., Teysseier, C., & Drury, M. R. (2020). Stress variations in space and time within the mantle section of an oceanic transform zone: Evidence for the seismic cycle. *Geology*, *48*(6), 569–573. <https://doi.org/10.1130/g47137.1>
- Chernak, L. J., & Hirth, G. (2010). Deformation of antigorite serpentinite at high temperature and pressure. *Earth and Planetary Science Letters*, *296*(1–2), 23–33. <https://doi.org/10.1016/j.epsl.2010.04.035>
- Chester, F. M., Rowe, C., Ujiie, K., Kirkpatrick, J., Regalla, C., Remitti, F., et al. (2013). Structure and composition of the plate-boundary slip zone for the 2011 Tohoku-Oki earthquake. *Science*, *342*(6163), 1208–1211. <https://doi.org/10.1126/science.1243719>
- Collettini, C., Niemeijer, A., Viti, C., Smith, S. A. F., & Marone, C. (2011). Fault structure, frictional properties and mixed-mode fault slip behavior. *Earth and Planetary Science Letters*, *311*(3–4), 316–327. <https://doi.org/10.1016/j.epsl.2011.09.020>
- Collettini, C., Viti, C., Smith, S. A. F., & Holdsworth, R. E. (2009). Development of interconnected talc networks and weakening of continental low-angle normal faults. *Geology*, *37*(6), 567–570. <https://doi.org/10.1130/g25645a.1>
- Constantin, M. (1999). Gabbroic intrusions and magmatic metasomatism in harzburgites from the Garrett transform fault: Implications for the nature of the mantle-crust transition at fast-spreading ridges. *Contributions to Mineralogy and Petrology*, *136*(1), 111–130. <https://doi.org/10.1007/s004100050527>
- Escartin, J., Hirth, G., & Evans, B. (1997). Nondilatant brittle deformation of serpentinites: Implications for Mohr-Coulomb theory and the strength of faults. *Journal of Geophysical Research*, *102*(B2), 2897–2913. <https://doi.org/10.1029/96JB02792>
- Escartin, J., Hirth, G., & Evans, B. (2001). Strength of slightly serpentinized peridotites: Implications for the tectonics of oceanic lithosphere. *Geology*, *29*(11), 1023–1026. [https://doi.org/10.1130/0091-7613\(2001\)029<1023:soospi>2.0.co;2](https://doi.org/10.1130/0091-7613(2001)029<1023:soospi>2.0.co;2)
- Escartin, J., Mével, C., MacLeod, C. J., & McCaig, A. M. (2003). Constraints on deformation conditions and the origin of oceanic detachments: The Mid-Atlantic Ridge core complex at 15°45'N. *Geochemistry, Geophysics, Geosystems*, *4*(8), 1–37. <https://doi.org/10.1029/2002gc000472>
- Evans, B. W. (2004). The serpentinite multisystem revisited: Chrysotile is metastable. *International Geology Review*, *46*(6), 479–506. <https://doi.org/10.2747/0020-6814.46.6.479>
- Fagereng, Å., & MacLeod, C. J. (2019). On seismicity and structural style of oceanic transform faults: A field geological perspective from the Troodos Ophiolite, Cyprus. In J. C. Duarte (Ed.), *Transform plate boundaries and fracture zones* (pp. 437–459). Elsevier.
- Fagereng, Å., & Sibson, R. H. (2010). Mélange rheology and seismic style. *Geology*, *38*(8), 751–754. <https://doi.org/10.1130/g30868.1>
- Fossen, H. (2016). *Structural geology*. Cambridge University Press.
- Fox, P. J., & Gallo, D. G. (1984). A tectonic model for ridge-transform-ridge plate boundaries: Implications for the structure of oceanic lithosphere. *Tectonophysics*, *104*(3–4), 205–242. [https://doi.org/10.1016/0040-1951\(84\)90124-0](https://doi.org/10.1016/0040-1951(84)90124-0)
- Froment, B., McGuire, J. J., van der Hilst, R. D., Gouédard, P., Roland, E. C., Zhang, H., & Collins, J. A. (2014). Imaging along-strike variations in mechanical properties of the Gofar transform fault, East Pacific Rise. *Journal of Geophysical Research: Solid Earth*, *119*(9), 7175–7194. <https://doi.org/10.1002/2014jb011270>
- Gass, I. G., MacLeod, C. J., Murton, B. J., Panayiotou, A., Simonian, K. O., & Xenophontos, C. (1994). The geological evolution of the Southern Troodos Transform Fault Zone, Cyprus (Vol. 9). Geological Survey Department.
- Grevemeyer, I., Hayman, N. W., Lange, D., Peirce, C., Papenberg, C., Van Avendonk, H. J. A., et al. (2019). Constraining the maximum depth of brittle deformation at slow- and ultraslow-spreading ridges using microseismicity. *Geology*, *47*(11), 1069–1073. <https://doi.org/10.1130/g46577.1>
- Handy, M. R. (1990). The solid-state flow of polymineralic rocks. *Journal of Geophysical Research*, *95*(B6), 8647–8661. <https://doi.org/10.1029/JB095iB06p08647>
- Hanks, T. C., & Kanamori, H. (1979). A moment magnitude scale. *Journal of Geophysical Research*, *84*(B5), 2348. <https://doi.org/10.1029/JB084iB05p02348>
- Hekinian, R., Bideau, D., Cannat, M., Francheteau, J., & Hébert, R. (1992). Volcanic activity and crust-mantle exposure in the ultrafast Garrett transform fault near 13°28'S in the Pacific. *Earth and Planetary Science Letters*, *108*(4), 259–275. [https://doi.org/10.1016/0012-821X\(92\)90027-S](https://doi.org/10.1016/0012-821X(92)90027-S)
- Hilalret, N., Reynard, B., Wang, Y., Daniel, I., Merkel, S., Nishiyama, N., & Petitgirard, S. (2007). High-pressure creep of serpentine, interseismic deformation and initiation of subduction. *Science*, *318*(318), 1910–1913. <https://doi.org/10.1029/JB084iB05p0234810.1126/science.1148494>
- Hirauchi, K.-I., Katayama, I., Uehara, S., Miyahara, M., & Takai, Y. (2010). Inhibition of subduction thrust earthquakes by low-temperature plastic flow in serpentine. *Earth and Planetary Science Letters*, *295*(3–4), 349–357. <https://doi.org/10.1016/j.epsl.2010.04.007>
- Hirauchi, K.-I., & Yamaguchi, H. (2007). Unique deformation processes involving the recrystallization of chrysotile within serpentinite: Implications for aseismic slip events within subduction zones. *Terra Nova*, *19*(6), 454–461. <https://doi.org/10.1111/j.1365-3121.2007.00771.x>
- Hirth, G., & Guillot, S. (2013). Rheology and tectonic significance of serpentinite. *Elements*, *9*(2), 107–113. <https://doi.org/10.2113/gselements.9.2.107>
- Holdsworth, R. E., Stewart, M., Imber, J., & Strachan, R. A. (2001). The structure and rheological evolution of reactivated continental fault zones: A review and case study. *Geological Society, London, Special Publications*, *184*(1), 115–137. <https://doi.org/10.1144/GSL.SP.2001.184.01.07>
- Homberg, C., Bergerat, F., Angelier, J., & Garcia, S. (2010). Fault interaction and stresses along broad oceanic transform zone: Tjörnes Fracture Zone, north Iceland. *Tectonics*, *29*(1). <https://doi.org/10.1029/2008tc002415>
- Ikari, M. J. (2015). Principal slip zones: Precursors but not recorders of earthquake slip. *Geology*, *43*(11), 955–958. <https://doi.org/10.1130/g37028.1>
- Imber, J., Holdsworth, R. E., Butler, C. A., & Lloyd, G. E. (1997). Fault-zone weakening processes along the reactivated Outer Hebrides Fault Zone, Scotland. *Journal of the Geological Society*, *154*(1), 105–109. <https://doi.org/10.1144/gsjgs.154.1.0105>
- Irwin, W. P., & Barnes, I. (1975). Effect of geologic structure and metamorphic fluids on seismic behavior of the San Andreas fault system in central and northern California. *Geology*, *3*(12), 713–716. [https://doi.org/10.1130/0091-7613\(1975\)3\(713:EOGSAM\)2.0.CO;2](https://doi.org/10.1130/0091-7613(1975)3(713:EOGSAM)2.0.CO;2)
- Kanamori, H., & Anderson, D. L. (1975). Theoretical basis of some empirical relations in seismology. *Bulletin of the Seismological Society of America*, *65*(5), 1073–1095.
- Karson, J. A., & Dick, H. J. B. (1983). Tectonics of ridge-transform intersections at the Kane fracture zone. *Marine Geophysical Researches*, *6*(1), 51–98. <https://doi.org/10.1007/BF00300398>
- Karson, J. A., Früh-Green, G. L., Kelley, D. S., Williams, E. A., Yoerger, D. R., & Jakuba, M. (2006). Detachment shear zone of the Atlantis Massif core complex, Mid-Atlantic Ridge, 30°N. *Geochemistry, Geophysics, Geosystems*, *7*(6). <https://doi.org/10.1029/2005GC001109>
- Kenkmann, T., & Dresen, G. (1998). Stress gradients around porphyroclasts: Palaeopiezometric estimates and numerical modelling. *Journal of Structural Geology*, *20*(2–3), 163–173. [https://doi.org/10.1016/S0191-8141\(97\)00074-6](https://doi.org/10.1016/S0191-8141(97)00074-6)

- Kohli, A. H., Goldsby, D. L., Hirth, G., & Tullis, T. (2011). Flash weakening of serpentinite at near-seismic slip rates. *Journal of Geophysical Research*, *116*(B3). <https://doi.org/10.1029/2010jb007833>
- Kohli, A. H., & Warren, J. M. (2020). Evidence for a deep hydrologic cycle on oceanic transform faults. *Journal of Geophysical Research: Solid Earth*, *125*(2). <https://doi.org/10.1029/2019jb017751>
- Kronenberg, A. K., Kirby, S. H., & Pinkston, J. (1990). Basal slip and mechanical anisotropy of biotite. *Journal of Geophysical Research*, *95*(B12), 19257–19278. <https://doi.org/10.1029/JB095iB12p19257>
- Kuna, V. M., Nábělek, J. L., & Braunmiller, J. (2019). Mode of slip and crust-mantle interaction at oceanic transform faults. *Nature Geoscience*, *12*(2), 138–142. <https://doi.org/10.1038/s41561-018-0287-1>
- MacLeod, C. J. (1988). *The tectonic evolution of the eastern Limassol Forest Complex, Cyprus* (Unpublished Ph.D. Thesis). The Open University.
- MacLeod, C. J. (1990). Role of the Southern Troodos Transform Fault in the rotation of the Cyprus microplate: Evidence from the Eastern Limassol Forest Complex. *Proceedings of the Symposium, Troodos 1987, Geological Survey Department* (pp. 75–85).
- MacLeod, C. J., Allerton, S., Gass, I. G., & Xenophontos, C. (1990). Structure of a fossil ridge-transform intersection in the Troodos Ophiolite. *Nature*, *348*(6303), 717–720. <https://doi.org/10.1038/348717a0>
- MacLeod, C. J., Escartín, J., Banerji, D., Banks, G. J., Gleeson, M., Irving, D. H. B., et al. (2002). Direct geological evidence for oceanic detachment faulting: The Mid-Atlantic Ridge, 15°45'N. *Geology*, *30*(10), 879–882. [https://doi.org/10.1130/0091-7613\(2002\)030<0879:DGEFOD>2.0.CO;2](https://doi.org/10.1130/0091-7613(2002)030<0879:DGEFOD>2.0.CO;2)
- MacLeod, C. J., & Murton, B. J. (1993). Structure and tectonic evolution of the Southern Troodos Transform Fault Zone, Cyprus. *Geological Society, London, Special Publications*, *76*(1), 141–176. <https://doi.org/10.1144/GSL.SP.1993.076.01.07>
- MacLeod, C. J., & Murton, B. J. (1995). On the sense of slip of the Southern Troodos Transform Fault Zone, Cyprus. *Geology*, *23*(3), 257–260. [https://doi.org/10.1130/0091-7613\(1995\)023<0257:OTSOSO>2.3.CO;2](https://doi.org/10.1130/0091-7613(1995)023<0257:OTSOSO>2.3.CO;2)
- McGuire, J. J., Collins, J. A., Gouédard, P., Roland, E., Lizarralde, D., Boettcher, M. S., et al. (2012). Variations in earthquake rupture properties along the Gofar transform fault, East Pacific Rise. *Nature Geoscience*, *5*(5), 336–341. <https://doi.org/10.1038/ngeo1454>
- Mével, C. (2003). Serpentinization of abyssal peridotites at mid-ocean ridges. *Comptes Rendus Geoscience*, *335*(10–11), 825–852. <https://doi.org/10.1016/j.crte.2003.08.006>
- Moore, D. E., Lockner, D. A., Ma, S., Summers, R., & Byerlee, J. D. (1997). Strengths of serpentinite gouges at elevated temperatures. *Journal of Geophysical Research*, *102*(B7), 14787–14801. <https://doi.org/10.1029/97JB00995>
- Moore, D. E., Lockner, D. A., Summers, R., Shengli, M., & Byerlee, J. D. (1996). Strength of chrysotile-serpentinite gouge under hydrothermal conditions: Can it explain a weak San Andreas Fault? *Geology*, *24*(11), 1041–1044. [https://doi.org/10.1130/0091-7613\(1996\)024<1041:SOCSGU>2.3.CO;2](https://doi.org/10.1130/0091-7613(1996)024<1041:SOCSGU>2.3.CO;2)
- Moore, D. E., Lockner, D. A., Tanaka, H., & Iwata, K. (2004). The coefficient of friction of chrysotile gouge at seismogenic depths. *International Geology Review*, *46*(5), 385–398. <https://doi.org/10.2747/0020-6814.46.5.385>
- Moore, D. E., & Rymer, M. J. (2007). Talc-bearing serpentinite and the creeping section of the San Andreas Fault. *Nature*, *448*(7155), 795–797. <https://doi.org/10.1038/nature06064>
- Moores, E. M., & Vine, F. J. (1971). The Troodos Massif, Cyprus and other ophiolites as oceanic crust: Evaluation and implications. *Philosophical Transactions of the Royal Society of London*, *268*(1192), 443–466. <https://doi.org/10.1098/rsta.1971.0006>
- Mukasa, S. B., & Ludden, J. N. (1987). Uranium-lead isotopic ages of plagiogranites from the Troodos Ophiolite, Cyprus, and their tectonic significance. *Geology*, *15*(9), 825–828. [https://doi.org/10.1130/0091-7613\(1987\)15<825:UIAOPF>2.0.CO;2](https://doi.org/10.1130/0091-7613(1987)15<825:UIAOPF>2.0.CO;2)
- Mumpton, F. A., & Thompson, C. S. (1975). Mineralogy and origin of the Coalinga asbestos deposit. *Clays and Clay Minerals*, *23*(2), 131–143. <https://doi.org/10.1346/CCMN.1975.0230209>
- Murton, B. J. (1986a). Anomalous oceanic lithosphere formed in a leaky transform fault: Evidence from the western Limassol Forest Complex, Cyprus. *Journal of the Geological Society*, *143*(5), 845–854. <https://doi.org/10.1144/gsjgs.143.5.0845>
- Murton, B. J. (1986b). *The tectonic evolution of the western Limassol Forest Complex, Cyprus* (Unpublished Ph.D. Thesis). The Open University.
- Nuriel, P., Katzir, Y., Abelson, M., Valley, J. W., Matthews, A., Spicuzza, M. J., & Ayalon, A. (2009). Fault-related oceanic serpentinization in the Troodos ophiolite, Cyprus: Implications for a fossil oceanic core complex. *Earth and Planetary Science Letters*, *282*(1–4), 34–46. <https://doi.org/10.1016/j.epsl.2009.02.029>
- O'Hanley, D. S. (1991). Fault-related phenomena associated with hydration and serpentine recrystallization during serpentinization. *The Canadian Mineralogist*, *29*(1), 21–35.
- O'Hanley, D. S., Chernosky, J. V., & Wicks, F. J. (1989). The stability of lizardite and chrysotile. *Canadian Mineralogist*, *27*(3), 483–493.
- Padrón-Navarta, J. A., Tommasi, A., Garrido, C. J., & López Sánchez-Vizcaíno, V. (2012). Plastic deformation and development of antigorite crystal preferred orientation in high-pressure serpentinites. *Earth and Planetary Science Letters*, *349*–350, 75–86. <https://doi.org/10.1016/j.epsl.2012.06.049>
- Parnell-Turner, R., Sohn, R. A., Peirce, C., Reston, T. J., MacLeod, C. J., Searle, R. C., & Simão, N. M. (2017). Oceanic detachment faults generate compression in extension. *Geology*, *45*(10), 923–926. <https://doi.org/10.1130/G39232.1>
- Pearce, J. A. (1975). Basalt geochemistry used to investigate past tectonic environments on Cyprus. *Tectonophysics*, *25*(1–2), 41–67. [https://doi.org/10.1016/0040-1951\(75\)90010-4](https://doi.org/10.1016/0040-1951(75)90010-4)
- Prigent, C., Warren, J. M., Kohli, A. H., & Teyssier, C. (2020). Fracture-mediated deep seawater flow and mantle hydration on oceanic transform faults. *Earth and Planetary Science Letters*, *532*(532), 115988–116013. <https://doi.org/10.1016/j.epsl.2019.115988>
- Reinen, L. A. (2000). Seismic and aseismic slip indicators in serpentinite gouge. *Geology*, *28*(2), 135–138. [https://doi.org/10.1130/0091-7613\(2000\)28<135:SAASII>2.0.CO;2](https://doi.org/10.1130/0091-7613(2000)28<135:SAASII>2.0.CO;2)
- Reinen, L. A., Weeks, J. D., & Tullis, T. E. (1991). The frictional behavior of serpentinite: Implications for aseismic creep on shallow crustal faults. *Geophysical Research Letters*, *18*(10), 1921–1924. <https://doi.org/10.1029/91GL02367>
- Reinen, L. A., Weeks, J. D., & Tullis, T. E. (1994). The frictional behavior of lizardite and antigorite serpentinites: Experiments, constitutive models, and implications for natural faults. *Pure and Applied Geophysics*, *143*(1), 317–358. <https://doi.org/10.1007/BF00874334>
- Reynard, B., Hilaiet, N., Balan, E., & Lazzeri, M. (2007). Elasticity of serpentines and extensive serpentinization in subduction zones. *Geophysical Research Letters*, *34*(13). <https://doi.org/10.1029/2007gl030176>
- Robertson, A. H. F. (1977). Tertiary uplift history of the Troodos massif, Cyprus. *Geological Society of America Bulletin*, *88*(12), 1763–1772. [https://doi.org/10.1130/0016-7606\(1977\)88<1763:TUHOTT>2.0.CO;2](https://doi.org/10.1130/0016-7606(1977)88<1763:TUHOTT>2.0.CO;2)
- Robertson, A. H. F., Parlak, O., & Ustaömer, T. (2012). Overview of the Palaeozoic-Neogene evolution of Neotethys in the Eastern Mediterranean region (Southern Turkey, Cyprus, Syria). *Petroleum Geoscience*, *18*(4), 381–404. <https://doi.org/10.1144/petgeo2011-091>

- Roland, E., Behn, M. D., & Hirth, G. (2010). Thermal-mechanical behavior of oceanic transform faults: Implications for the spatial distribution of seismicity. *Geochemistry, Geophysics, Geosystems*, *11*(7). <https://doi.org/10.1029/2010gc003034>
- Rooney, J. S., Tarling, M. S., Smith, S. A. F., & Gordon, K. C. (2018). Submicron Raman spectroscopy mapping of serpentinite fault rocks. *Journal of Raman Spectroscopy*, *49*(2), 279–286. <https://doi.org/10.1002/jrs.5277>
- Roum jon, S., Cannat, M., Agrinier, P., Godard, M., & Andreani, M. (2015). Serpentinization and fluid pathways in tectonically exhumed peridotites from the Southwest Indian Ridge (62–65 E). *Journal of Petrology*, *56*(4), 703–734. <https://doi.org/10.1093/petrology/egv014>
- Roum jon, S., Williams, M. J., & Fr uh-Green, G. L. (2018). In-situ oxygen isotope analyses in serpentine minerals: Constraints on serpentinization during tectonic exhumation at slow- and ultraslow-spreading ridges. *Lithos*, *323*, 156–173. <https://doi.org/10.1016/j.lithos.2018.09.021>
- Rutter, E. H. (1976). The kinetics of rock deformation by pressure solution. *Philosophical Transactions of the Royal Society of London*, *283*, 203–219. <https://doi.org/10.1098/rsta.1976.0079>
- Schleicher, A. M., van der Pluijm, B. A., & Warr, L. N. (2012). Chlorite-smectite clay minerals and fault behavior: New evidence from the San Andreas Fault Observatory at Depth (SAFOD) core. *Lithosphere*, *4*(3), 209–220. <https://doi.org/10.1130/1158.1>
- Scholz, C. H. (1998). Earthquakes and friction laws. *Nature*, *391*(6662), 37–42. <https://doi.org/10.1038/34097>
- Scholz, C. H. (2002). *The mechanics of earthquake faulting* (2nd ed., pp. 1–467). Cambridge University Press.
- Shervais, J. W., Kolesar, P., & Andreasen, K. (2005). A field and chemical study of serpentinization-stonyford, California: Chemical flux and mass balance. *International Geology Review*, *47*(1), 1–23. <https://doi.org/10.2747/0020-6814.47.1.1>
- Simonian, K. O. (1975). *The geology of the Arakapas Fault Belt area, Troodos Massif, Cyprus* (Unpublished Ph.D. Thesis). The Open University.
- Simonian, K. O., & Gass, I. G. (1978). Arakapas Fault Belt, Cyprus: A fossil transform fault. *Geological Society of America Bulletin*, *89*(8), 1220–1230. [https://doi.org/10.1130/0016-7606\(1978\)89\(1220:AFBCAF\)2.0.CO;2](https://doi.org/10.1130/0016-7606(1978)89(1220:AFBCAF)2.0.CO;2)
- Smith, S. A. F., Holdsworth, R. E., Collettini, C., & Pearce, M. A. (2011). The microstructural character and mechanical significance of fault rocks associated with a continental low-angle normal fault: The Zuccale Fault, Elba Island, Italy. *Geological Society, London, Special Publications*, *359*(1), 97–113. <https://doi.org/10.1144/sp359.6>
- Tarling, M. S., Smith, S. A. F., Scott, J. M., Rooney, J. S., Viti, C., & Gordon, K. C. (2019). The internal structure and composition of a plate boundary-scale serpentinite shear zone: The Livingstone Fault, New Zealand. *Solid Earth Discussions*, *10*(4), 1025–1047. <https://doi.org/10.5194/se-2019-62>
- Tarling, M. S., Smith, S. A. F., Viti, C., & Scott, J. M. (2018). Dynamic earthquake rupture preserved in a creeping serpentinite shear zone. *Nature Communications*, *9*(1), 3552. <https://doi.org/10.1038/s41467-018-05965-0>
- Tesei, T., Harbord, C. W. A., De Paola, N., Collettini, C., & Viti, C. (2018). Friction of mineralogically controlled serpentinites and implications for fault weakness. *Journal of Geophysical Research: Solid Earth*, *123*(8), 6976–6991. <https://doi.org/10.1029/2018jb016058>
- Vannucchi, P., Maltman, A., Bettelli, G., & Clennell, B. (2003). On the nature of scaly fabric and scaly clay. *Journal of Structural Geology*, *25*(5), 673–688. [https://doi.org/10.1016/S0191-8141\(02\)00066-4](https://doi.org/10.1016/S0191-8141(02)00066-4)
- Varga, R. J., & Moores, E. M. (1985). Spreading structure of the Troodos ophiolite, Cyprus. *Geology*, *13*(12). [https://doi.org/10.1130/0091-7613\(1985\)13\(846:Sotto\)2.0.Co;2](https://doi.org/10.1130/0091-7613(1985)13(846:Sotto)2.0.Co;2)
- Viti, C., Collettini, C., Tesei, T., Tarling, M., & Smith, S. (2018). Deformation processes, textural evolution and weakening in retrograde serpentinites. *Minerals*, *8*(6), 241. <https://doi.org/10.3390/min8060241>
- Viti, C., & Mellini, M. (1998). Mesh textures and bastites in the Elba retrograde serpentinites. *European Journal of Mineralogy*, *10*(6), 1341–1360. <https://doi.org/10.1127/ejm/10/6/1341>
- Warren, J. M., & Hirth, G. (2006). Grain size sensitive deformation mechanisms in naturally deformed peridotites. *Earth and Planetary Science Letters*, *248*(1–2), 438–450. <https://doi.org/10.1016/j.epsl.2006.06.006>
- Wassmann, S., St ockhert, B., & Trepmann, C. A. (2011). Dissolution precipitation creep versus crystalline plasticity in high-pressure metamorphic serpentinites. *Geological Society, London, Special Publications*, *360*(1), 129–149. <https://doi.org/10.1144/sp360.8>
- Wells, D. L., & Coppersmith, K. J. (1994). New empirical relationships among magnitude, rupture length, rupture width, rupture area, and surface displacement. *Bulletin of the Seismological Society of America*, *84*(4), 974–1002.
- Wicks, F. J., & Whittaker, E. J. W. (1977). Serpentine textures and serpentinization. *The Canadian Mineralogist*, *15*(4), 459–488.
- Wolfson-Schwehr, M., Boettcher, M. S., McGuire, J. J., & Collins, J. A. (2014). The relationship between seismicity and fault structure on the Discovery transform fault, East Pacific Rise. *Geochemistry, Geophysics, Geosystems*, *15*(9), 3698–3712. <https://doi.org/10.1002/2014gc005445>